Optimized pulses for the control of uncertain qubits

Matthew D. Grace*
Department of Scalable & Secure Systems Research, Sandia National Laboratories, Livermore, California 94550, USA

Jason M. Dominy†
Program in Applied & Computational Mathematics, Princeton University, Princeton, New Jersey 08544, USA

Wayne M. Witzel‡
Department of Advanced Device Technologies, Sandia National Laboratories, Albuquerque, New Mexico 87185, USA

Malcolm S. Carroll§
Department of Photonic Microsystem Technologies, Sandia National Laboratories, Albuquerque, New Mexico 87185, USA

(Received 11 May 2011; revised manuscript received 19 January 2012; published 18 May 2012)

Constructing high-fidelity control fields that are robust to control, system, and/or surrounding environment uncertainties is a crucial objective for quantum information processing. Using the two-state Landau-Zener model for illustrative simulations of a controlled qubit, we generate optimal controls for $\pi/2$ and π pulses and investigate their inherent robustness to uncertainty in the magnitude of the drift Hamiltonian. Next, we construct a quantum-control protocol to improve system-drift robustness by combining environment-decoupling pulse criteria and optimal control theory for unitary operations. By perturbatively expanding the unitary time-evolution operator for an open quantum system, previous analysis of environment-decoupling control pulses has calculated explicit control-field criteria to suppress environment-induced errors up to (but not including) third order from $\pi/2$ and π pulses. We systematically integrate this criteria with optimal control theory, incorporating an estimate of the uncertain parameter to produce improvements in gate fidelity *and* robustness, demonstrated via a numerical example based on double quantum dot qubits. For the qubit model used in this work, *postfacto* analysis of the resulting controls suggests that realistic control-field fluctuations and noise may contribute just as significantly to gate errors as system and environment fluctuations.

DOI: 10.1103/PhysRevA.85.052313 PACS number(s): 03.67.−a, 02.30.Yy

I. INTRODUCTION

Demanding requirements for gate fidelities to achieve fault-tolerant quantum computation (QC) [1] have motivated the need for improved quantum control protocols (QCPs). In quantum information science [2], there are (at least) three distinct dynamical approaches to improving the fidelity of qubit operations in the presence of environmental interactions: dynamical-decoupling (DD) pulse sequences [3,4], optimal control theory (OCT) [5,6], and quantum error-correcting codes (QECCs) [1]. Although interesting nondynamical methods exist for noise suppression, such as decoherence-free subspaces (DFSs) [7], noiseless subsystems [8], and anyonic or topological systems [9], the work reported in this article focuses exclusively on dynamical approaches for controlling quantum systems [10]. Specifically, the objective of this work is to construct a *hybrid* QCP, combining methods and results from DD and OCT, to locate control fields that (a) produce high-fidelity rotations about a particular axis *and* (b) are robust with respect to an uncertain frequency of rotation about an orthogonal axis. By combining complementary features of these analytically and numerically based QCPs, we have developed a hybrid QCP where estimates of system parameters can be directly incorporated into numerical simulations to generate improved quantum operations.

During the past few years, P. Karbach, S. Pasini, G. Uhrig, and colleagues have made significant contributions toward the mathematical analysis and design of DD pulses and sequences for controlling qubit systems and decoupling them from their surrounding environment (see, e.g., Refs. [4,11–17]). In a recent article [15], using a rather general open-system, time-dependent Hamiltonian for one qubit, they derive analytical control-field criteria for $\pi/2$ and π pulses, which, when satisfied, eliminate the first- and second-order errors in the unitary time-evolution operator resulting from qubit-environment interactions. In this work, we refer to these criteria as "decoupling-pulse criteria" (DPC) and to the control fields that satisfy this criteria as "decoupling pulses" (DPs). We adapt the DPC for the case of closed-system unitary control, where the dynamics are influenced by an uncertain drift (i.e., time-independent) term in the qubit Hamiltonian. For control fields that satisfy the DPC, this adaptation eliminates the first- and second-order effects resulting from the drift term. Using a novel method for multiobjective control, we combine the mathematical DPC with a numerical procedure based on OCT for unitary control [18] that incorporates an estimate of the drift-term magnitude (i.e., system information) to construct control fields with increased fidelity and robustness to uncertainty in the drift term. For brevity, we refer to this combination

*mgrace@sandia.gov
†Present address: Center for Quantum Information Science, and Technology, University of Southern California, Los Angeles, California 90089, USA; jdominy@usc.edu
‡wwitzel@sandia.gov
§mscarro@sandia.gov

of the DPC and OCT as "DPC + OCT." To demonstrate the utility of our approach, we optimize and evaluate these control fields using a qubit model based on the two-level Landau-Zener Hamiltonian [19] that has an uncertain drift term and is driven by a deterministic control field. Even though the qubit model is quite general (i.e., the Hamiltonian employed represents a one-qubit system with a linear drift term, driven by a scalar control field) and thus describes a variety of qubits (e.g., atomic, spin, superconducting, etc. [2]), we select physical units for the model that are relevant to double quantum dot (DQD) qubits to investigate the practical features of our results [20]. With this model system, we demonstrate that the DPC + OCT combination can be used to produce (a) improved fidelity compared to DPs alone and (b) improved robustness to uncertainty in the drift magnitude compared to results from DPs and OCT alone. Although research examining the effects of classical control noise is *extremely* important for practical QC [21,22], all control fields in this work are assumed to be deterministic, with control amplitudes that are exact to numerical precision. Thus, uncertainty is assumed to be present only in the system and, unless otherwise specified, control robustness refers to robustness to drift uncertainty.

Related research on hybrid QCPs includes that performed by Lidar *et al*., who proposed the application of DD pulse sequences on *logical* qubits encoded in DFSs or QECCs to eliminate decoherence in solid-state and trapped-ion qubits [23–26]. Borneman *et al*. used OCT to design control fields that are robust to systematic amplitude and resonance inhomogeneities, thereby improving the performance of the so-called Carr-Purcell-Meiboom-Gill pulse sequence [27]. In addition, there have been many studies on the control and controllability of (inhomogeneous) quantum mechanical ensembles, such as a collection of coupled or uncoupled spin systems, primarily for state-based objectives (see, e.g., Refs. [28–32]), and sequences of unitary time-evolution operators that compensate for systematic off-resonant effects (see, e.g., [33–37]).

This article is organized as follows: Section II introduces and develops the model qubit system based on the Landau-Zener Hamiltonian [19] used in our optimizations and simulations. For illustrative purposes, this model is compared to a logical DQD semiconductor qubit, where uncertainty in the drift term of the system Hamiltonian is due to the surrounding nuclear spin environment [38,39]. A system of scaled units is defined that allows for the comparison of our model and control fields to relevant experimental parameters. In Sec. III, we summarize our gradient-based OCT routine for deterministic Hamiltonian systems, describing our objective functional for unitary control, relevant control properties, and the numerical optimization procedure. Section IV presents results from unitary OCT for subsequent comparison to those from the DPC and DPC + OCT QCPs. Inherent robustness of these optimal controls (OCs) to variations in the magnitude of the uncertain drift term is also analyzed, and a functional is proposed to quantify this robustness. For the individual unitary targets considered, despite the similar structures of the resulting OCs for different drift-term magnitudes, their gate distances as a function of the drift magnitude differ dramatically. Section V summarizes the nonlinear control-field criteria developed by Pasini *et al*. for designing control pulses that are robust to decoherence [15]. Our adaptation of these criteria to closed-system unitary control is explained and the hybrid DPC + OCT control problem is posed. Control fields satisfying this criteria are applied to our model qubit system and their robustness is analyzed. In Sec. VI, we describe and mathematically formulate our gradient-based method for solving the nonlinearly constrained control problem. Section VII presents results from our DPC + OCT optimization algorithm. Gate distance and robustness of the control fields are numerically analyzed and discussed. We also compare OCT, DPC, and DPC + OCT results collectively to illustrate the benefit of our hybrid approach. In addition to comparing the gate distances directly, we apply these controls to an inhomogeneous ensemble of systems to emphasize the improvement that may be obtained from this hybrid QCP. Like the OCT results, significant gate-distance sensitivities to relatively small control-field differences are observed for the DPC + OCT controls, supporting further study and suppression of the effects of undesired control-field fluctuations and noise on quantum information processing. We conclude this article in Sec. VIII with a summary of our results and identify several future directions of our research.

II. LANDAU-ZENER MODEL SYSTEM

A. Model Hamiltonian

We represent the dynamical model of a qubit with the following Hamiltonian (where $\hbar = 1$; details regarding units appear in Sec. II C):

$$H(t) := \varepsilon S_x + C(t) S_z, \tag{1}$$

where $S_\lambda := \sigma_\lambda/2$ is a spin operator for a spin-1/2 particle, σ_λ is a Pauli matrix ($\lambda \in \{x, y, z\}$), εS_x represents a persistent rotation about the x axis, and $C(t)$ represents the time-dependent control field driving rotations about the z axis. Note that $H(t)$ corresponds to the two-state Landau-Zener model [19], and that both $C(t)/\hbar$ and $\varepsilon/\hbar$ have units of angular frequency (e.g., radians per second in SI units).

Let $\mathcal{H}$ denote the Hilbert space of the system, where $n := \dim\{\mathcal{H}\}$ ($n = 2$ for one qubit), and $\{|\mathcal{S}_i\rangle\}$ denote the orthonormal basis of S_z that spans $\mathcal{H}$, with corresponding eigenvalues $\pm 1/2$. The Lie group of all unitary operators on $\mathcal{H}$ is denoted by $\mathrm{U}(\mathcal{H})$. In general, the unitary time-evolution operator $U(t) \in \mathrm{U}(\mathcal{H})$ for a closed quantum system obeys the time-dependent Schrödinger equation

$$\dot{U}(t) = -i H(t) U(t), \tag{2}$$

where $U(t = 0) = \mathbb{1}_n$, the $n \times n$ identity matrix. From a controllability perspective [40,41], the Hamiltonian in Eq. (1) generates the Lie algebra su(2). Thus, the system is completely dynamically controllable; that is, any element of the Lie group SU(2) can be generated via Eq. (2) and an appropriately shaped control field. However, this analysis does not necessarily reveal anything about the control-field structure required to realize an arbitrary SU(2) operation. As an illustrative example of our DPC + OCT QCP, we focus on constructing unitary operations corresponding to $\pi/2$ and π rotations about the z axis.

B. Double quantum dot logical qubit

Although our qubit model is quite general, for illustrative purposes we refer to a particular application of a DQD solid-state qubit [42,43], which has been studied in an array of experiments (see, e.g., [44–48]). With one electron in each quantum dot, the DQD system spans four spin-1/2 states. An applied magnetic field will break the degeneracy of the states in which both electrons are either aligned against or with the field. In this situation, it is possible (and often advantageous) to work within the two-level subspace where the net spin angular momentum is zero. By adjusting voltages in the electrostatically defined quantum dots, the magnitude of the exchange interaction between the electrons may be controlled. This interaction controls the splitting between the singlet $|S\rangle := (|\uparrow\downarrow\rangle - |\downarrow\uparrow\rangle)/\sqrt{2}$ and triplet $|T_0\rangle := (|\uparrow\downarrow\rangle + |\downarrow\uparrow\rangle)/\sqrt{2}$ states of the spin-zero manifold. Designating $|\mathcal{S}_0\rangle = |S\rangle$ and $|\mathcal{S}_1\rangle = |T_0\rangle$, we equate $C(t)$ in our general model [Eq. (1)] with the exchange interaction.

The spin-zero manifold is insensitive to a global magnetic field. However, gradients in the magnetic field will cause singlet-triplet transitions. Such a gradient splits the energy of the states $|\uparrow\downarrow\rangle = (|T_0\rangle + |S\rangle)/\sqrt{2}$ and $|\downarrow\uparrow\rangle = (|T_0\rangle - |S\rangle)/\sqrt{2}$ by the difference in effective Zeeman energies for an electron in either of the two quantum dots. In this context, we may therefore equate the energy ε with this effective Zeeman-energy difference. In GaAs DQD systems, the effective Zeeman-energy difference is typically dominated by the Overhauser shifts from a lattice of randomly polarized nuclear spins corresponding to approximately 1.602×10^{-26} to 1.602×10^{-25} J (or 10^{-7} to 10^{-6} eV) [42,43]. It has been demonstrated that a desired difference in Overhauser shift of a GaAs DQD may be realized through feedback control from a preparatory qubit [48]. However, the value of ε will drift over time through the nuclear spin diffusion that causes spectral diffusion [3,38,39,49], motivating the need for robust control. In proposed Si DQD systems (see, e.g., Ref. [50]), nuclear spins may be eliminated through isotopic enrichment. Other spin baths, such as electron spins of donor impurities [51] or dangling bond spins at an interface [52], may also lead to variations and drift in the value of ε.

C. Scaled-unit system

In addition to setting the reduced Planck constant $\hbar = 1$ (corresponding to unit of angular momentum: energy × time), a simple set of scaled units is defined by also setting the final time of the controlled evolution $t_f = 1$. The ratio $\hbar/t_f = 1$ yields the scaled unit of energy, which, when $t_f = 20$ ns (as an example), corresponds to approximately 5.273×10^{-27} J (or 3.291×10^{-8} eV). By appropriately scaling the Hamiltonian and control field, this propagation time can be transformed to any final time t_f. Relationships between these scaled units and SI units (when $t_f = 20$ ns) are summarized in Table I.

In this work, optimizations were performed for individual values of $\varepsilon \in [0,5]$; we denote the nominal values of ε used in these calculations as ε_0. This range of ε corresponds to zero and moderate rotations from the environment for the GaAS DQD example. For a DQD logical qubit,

$$\varepsilon = g_e \mu_B B_\Delta, \tag{3}$$

TABLE I. Scaled and SI units for the logical qubit described by the Hamiltonian in Eq. (1).

Physical quantity	Scaled unit	SI unit
Angular momentum: $\hbar$	1	1.055×10^{-34} J s
Time: t	1	2.0×10^{-8} s
Energy: C, ε	1	5.273×10^{-27} J

where g_e is the so-called electron g factor, μ_B is the Bohr magneton, and B_Δ is the magnetic field resulting from the difference in the random hyperfine fields from each quantum dot along the direction of the applied field. When 1 scaled unit of time corresponds to 20 ns (a representative estimate of the time required for one-qubit rotations for a DQD system [45,53]), $\varepsilon = 5$ scaled units of angular frequency (the maximum value of ε_0 considered) corresponds to $B_\Delta \approx 6.5$ mT; this is consistent with experimental reports of GaAs DQDs (where $g_e = -0.44$) [42,43,45]. Unless stated otherwise, all physical quantities in this work are expressed in scaled units.

III. OPTIMAL CONTROL OF UNITARY OPERATIONS VIA GRADIENT-BASED ALGORITHMS

A. Objective functionals for unitary operations

For a target unitary operation $V \in \mathrm{U}(\mathcal{H})$, the distance Δ between V and a simulated final-time unitary operation $U(t_f)$ is

$$\Delta[V, U(t_f; C)] := \min_{\varphi \in \mathbb{R}} \frac{1}{\sqrt{2n}} \|U(t_f; C) - \exp(i\varphi) V\|_{\mathrm{HS}} \tag{4a}$$

$$= \sqrt{1 - \frac{1}{n} |\mathrm{Tr}[V^\dagger U(t_f)]|}, \tag{4b}$$

where $\|\cdot\|_{\mathrm{HS}}$ denotes the norm based on the Hilbert-Schmidt inner product: $\langle A, B\rangle_{\mathrm{HS}} := \mathrm{Tr}(A^\dagger B)$, $A, B \in \mathcal{M}_n(\mathbb{C})$ [$\mathcal{M}_n(\mathbb{X})$ denotes the set of $n \times n$ matrices over the field $\mathbb{X}$]. This *phase-invariant* distance measure is a special case of a more general distance measure developed in Ref. [54], which is applicable to studies involving composite systems where only the qubit (system) dynamics are directly of interest [55,56].

Concerning mathematical notation, because the unitary time-evolution operator is a function of time and a functional of the control, it will be expressed more generally as $U(t; C)$ for all time t and a control C, compared to $U(t)$; the final-time unitary operator will be expressed more generally as $U_{t_f}(C)$, compared to $U(t_f)$. Also, we denote the space of admissible controls with final time $t = t_f$ as $\mathfrak{C}_{t_f}$. Some properties of the Hilbert space $\mathfrak{C}_{t_f}$ are discussed below; further details are in Ref. [54].

Because $0 \leqslant \Delta \leqslant 1$ in general, it is useful to define the fidelity $\mathcal{F}$ of unitary operations as [54,57]

$$\mathcal{F} := \frac{1}{n} |\mathrm{Tr}[V^\dagger U(t_f)]| = 1 - \Delta^2\big(V, U_{t_f}\big), \tag{5}$$

which is a common phase-invariant measure of gate fidelity based on the Hilbert-Schmidt inner product (see, e.g., Refs. [18,58,59]). Note the quadratic dependence of $\mathcal{F}$ on Δ (i.e., a distance of 10^x corresponds to a fidelity of $1 - 10^{2x}$, where $x \leqslant 0$).

An optimal control field for a given unitary operation may be located by minimizing an objective functional $\mathcal{J}[C]$ of the control field that incorporates the final-time unitary target V, constrains the dynamics of $U(t)$ to evolve according to Eq. (2), and penalizes the fluence of the control field. For this work, the objective functional is defined as

$$\mathcal{J}[C] := \Delta\big[V, U_{t_f}(C)\big] + \frac{\alpha}{2}\int_0^{t_f} \frac{C^2(t)}{s(t)}dt. \tag{6}$$

Often, the minimization of $\mathcal{J}$ is performed using a gradient-based algorithm (GrA; see [18,54,55,60] for details and examples of gradient-based optimizations). Here, $\alpha \geqslant 0$ weighs the control-field fluence relative to the distance Δ and $s : [0,t_f] \mapsto \mathbb{R}$ is a continuous "shape function." When appropriately chosen, $s(t)$ penalizes undesirably shaped functions [54]. We use $s(t) = \sin^p(\pi t/t_f)$, where $p \in \mathbb{Q}_+ \cup \{0\}$. For $p \neq 0$, this form penalizes the control-field slew rate around the initial and final times and favors controls where $C(0) = C(t_f) = 0$.

For the time-dependent Hamiltonian in Eq. (1), $U_{t_f} : \mathfrak{C}_{t_f} \to \mathrm{U}(\mathcal{H})$ denotes the map, defined implicitly through the Schrödinger equation [Eq. (2)], that takes a control field $C \in \mathfrak{C}_{t_f}$ to the final-time unitary evolution operator $U_{t_f} \in \mathrm{U}(\mathcal{H})$. Note that $\mathfrak{C}_{t_f}$ is a Hilbert space of admissible controls, on which $U(t;C)$ exists for all $t \in [0,t_f]$ and all $C \in \mathfrak{C}_{t_f}$ [61], where the inner product on $\mathfrak{C}_{t_f}$ is

$$\langle f,g\rangle_{\mathfrak{C}_{t_f}} := \int_0^{t_f} \frac{f(t)g(t)}{s(t)}dt \;\forall\; f,g \in \mathfrak{C}_{t_f}. \tag{7}$$

As such, $\mathcal{J} : \mathfrak{C}_{t_f} \to \mathbb{R}$ is the *dynamical* version of the distance measure Δ, with a relative cost on the control-field fluence, determined by α. The role of the shape function $s(t)$ in Eqs. (6) and (7) is to change the geometry of control space, moving undesirably shaped functions away from the origin, out to infinity, where they are less likely to be the targets of a minimization over $\mathfrak{C}_{t_f}$ [54].

B. Control rotation angle $\theta(t;C)$

In addition to the objective functional $\mathcal{J}$ and inner product on $\mathfrak{C}_{t_f}$, another important expression is the integral of the control field:

$$\theta(t;C) := \int_0^t C(\tau)d\tau. \tag{8a}$$

The angle θ corresponds to the rotation about the z axis performed by the control field during the time interval $[0,t]$. Although θ is a functional of the control field $C(t)$, whenever appropriate we abbreviate $\theta(t;C)$ as $\theta(t)$ to avoid unnecessarily cumbersome notation. Equation (8a) is equivalent to

$$\frac{d\theta(t;C)}{dt} = C(t). \tag{8b}$$

Also,

$$\frac{\delta\theta[t;C]}{\delta C(t')} = \mathfrak{H}(t-t') \tag{8c}$$

(i.e., the functional derivative of θ with respect to C), where $\mathfrak{H}(t-t')$ is the Heaviside step function:

$$\mathfrak{H}(t'-t) := \begin{cases} 1 & \text{when} \quad t \geqslant t' \\ 0 & \text{when} \quad t < t'. \end{cases} \tag{9}$$

C. Optimization with gradient-based algorithm

This section briefly summarizes the variational analysis of $\mathcal{J}$ and describes criteria for the optimal points (or submanifolds) of $\mathcal{J}$ with respect to a control field C. The gradient of the objective functional $\mathcal{J}$ is explicitly derived in Ref. [54]; we present it here for continuity:

$$(\nabla\mathcal{J}[C])(t) = \frac{s(t)}{4n\,\Delta[V,U_{t_f}(C)]}\mathrm{Im}\big(\mathrm{Tr}\big\{\big[U_{t_f}^\dagger(C)R - R^\dagger U_{t_f}(C)\big] \times U^\dagger(t;C)S_z U(t;C)\big\}\big) + \alpha C(t), \tag{10}$$

where $R := \exp(i\varphi)V$ and $\varphi := \mathrm{Im}\{\ln[\mathrm{Tr}(V^\dagger U_{t_f})]\}$. Critical points of $\mathcal{J}$ (a real-valued functional) are defined as controls for which $(\nabla\mathcal{J}[C])(t) = 0$ for all time t [62]. Control fields are iteratively updated using this gradient to improve the value of the objective functional $\mathcal{J}$. Given the kth iterate of the control field $C^{(k)}(t)$, adjustments to the control field for the $(k+1)$th iteration are given by

$$C^{(k+1)}(t) := C^{(k)}(t) - \beta(\nabla\mathcal{J}[C^{(k)}])(t), \tag{11}$$

where β is a constant that determines the magnitude of the field adjustment. This procedure describes an implementation of a steepest-descent algorithm [63]. In this work, initial control fields $C^{(0)}$ are continuous approximations to simple square-wave pulses, where initial and final times and slew rates are consistent with the shape function $s(t) = \sin(\pi t/t_f)$.

IV. RESULTS FROM QUANTUM OPTIMAL CONTROL THEORY

Using *only* the GrA presented in Sec. III, OCs were found for unitary targets that perform $\pi/2$ and π rotations about the z axis:

$$Z_\phi := \begin{pmatrix} \exp(-i\phi/2) & 0 \\ 0 & \exp(i\phi/2) \end{pmatrix}, \tag{12}$$

where $\phi \in \{\pi/2,\pi\}$. The final time for all OCs was fixed at $t_f = 1$ scaled unit of time. With the GrA and the objective functional $\mathcal{J}$, a combination of the value of ε and the structure of the initial control field determines the resulting optimal control field. Optimizations were performed individually for *specific* angular frequencies: $\varepsilon_0 \in [0,5]$. As described in Sec. II C, this interval represents the regime of zero to moderate rotation from the environment for the DQD logical qubit. To emphasize the ε-specific nature of these OCs, we denote them as $C_o(\varepsilon_0;t)$.

Because of the similarity of results over the entire interval $0 \leqslant \varepsilon \leqslant 5$, only a subset will be presented. OC fields for $Z_{\pi/2}$ and Z_π as a function of ε are presented in Figs. 1 and 2, respectively, for $\varepsilon_0 \in \{0,1,2,3,4,5\}$. Even though all of these OCs were located using the same initial control field, which is very similar to the OC reported for $\varepsilon_0 = 0$ for both targets, some of the converged fields differ dramatically for different values of ε_0. All OCs have distances $\Delta < 10^{-6}$ (or $\mathcal{F} > 1 - 10^{-12}$, essentially corresponding to the limits of numerical precision), which is expected because this system is relatively simple and fully controllable [40,41]. For $\varepsilon_0 = 0$, all OCs for Z_ϕ satisfy $\theta(t_f) \equiv \phi \pmod{2\pi}$ (i.e., OC design simply corresponds to pulse-area control in this situation). However, when $\varepsilon \neq 0$, there is no corresponding pulse-area requirement.

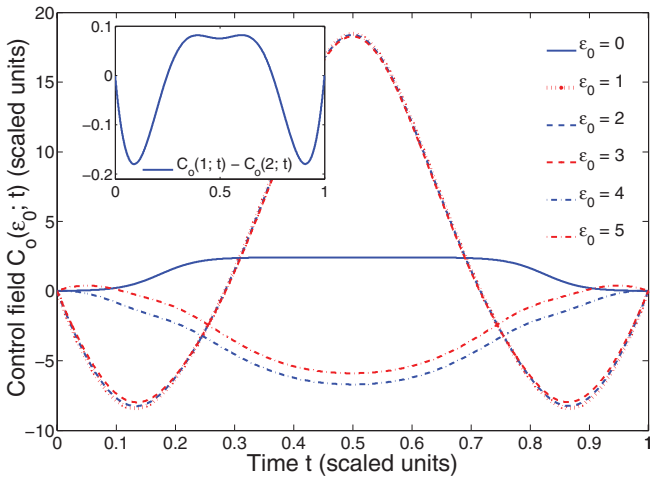

FIG. 1. (Color online) OC fields producing a $Z_{\pi/2}$ operation for several *specific* values of ε_0 and $t_f = 1$ scaled unit. All OCs have distances $\Delta(Z_{\pi/2}, U_{t_f}) \leqslant 10^{-6}$. The inset presents the difference between $C_o(1;t)$ and $C_o(2;t)$. Although distinct, note that $C_o(1;t)$, $C_o(2;t)$, and $C_o(3;t)$ appear nearly indistinguishable in this figure.

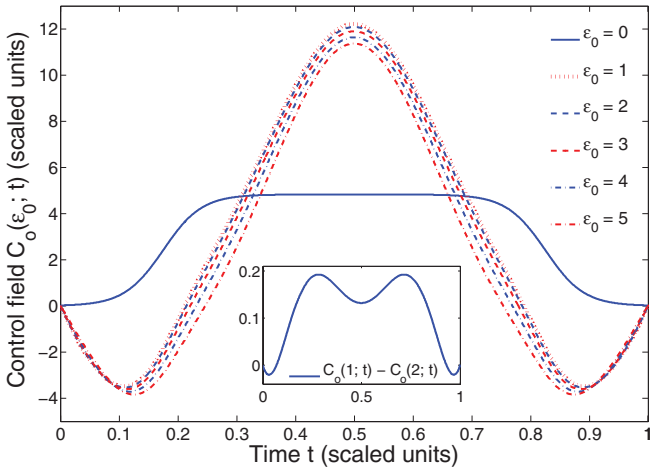

FIG. 2. (Color online) OC fields producing a Z_π operation for several *specific* values of ε_0 and $t_f = 1$ scaled unit. All OCs have distances $\Delta(Z_\pi, U_{t_f}) < 10^{-6}$. The inset presents the difference between $C_o(1;t)$ and $C_o(2;t)$.

In fact, if ε is known accurately, it is possible to perform Z_ϕ operations with piecewise constant controls that satisfy $\theta(t_f) = 0$. Table II contains information about some of the properties of these OCs. For a DQD logical qubit, we observe that these controls require negative exchange coupling values. Although negative exchange energy is uncommon, it is predicted to be possible to produce through combined tuning of the magnetic field, dot size, and tunnel coupling [64].

For both $Z_{\pi/2}$ and Z_π operations, despite the similar structures of the OCs, especially $C_o(1;t)$ and $C_o(2;t)$, their gate-distance responses for $0 \leqslant \varepsilon \leqslant 6$ (with a numerical resolution of 0.01 scaled units) are quite unique, as shown in Figs. 3 and 4, respectively. Even though $\max_t \|C_o(1;t) - C_o(2;t)\| < 0.2$ scaled units of energy for both operations (see inset of Figs. 1 and 2), and the mean relative difference is approximately 1.4% and 5.7% for the $Z_{\pi/2}$ and Z_π operations, respectively, this two-level system effectively discriminates between these two similar control fields through the response of the distance functional Δ in Eq. (4). Within the interval $0 \leqslant \varepsilon \leqslant 3$, the gate distances of $C_o(1;t)$ and $C_o(2;t)$ do not significantly overlap. The sensitivity of this system to these relatively small control-field variations combined with the inherent noise (and limited resolution) present in most realistic control sources warrants further study of the impact that realistic control-field fluctuations may have on practical fault-tolerant QC [20,50,58,65].

For the target operation $Z_{\pi/2}$, when $\varepsilon_0 \in \{0,1,2,3\}$, the OCs produce a net positive angle of rotation about the z axis, given the initial control field. When $\varepsilon_0 \in \{4,5\}$, OCs produce a net negative angle of rotation about the z axis. As the static angular frequency of the rotation about the x axis increases, the OC strategy tends toward a controlled rotation about the z axis in the negative direction. OC simulations for $3 \leqslant \varepsilon_0 \leqslant 4$, with a numerical resolution of 0.01 scaled units of energy (detailed results are not reported), reveal a distinct transition

TABLE II. Performance of the OCs $C_o(\varepsilon_0;t)$ for one-qubit Z_ϕ operations. Here, $\max|C_o|$, θ, $\Phi[C] := \int_0^{t_f} C^2(\varepsilon_0;t)dt$, Δ, and $\mathcal{R}_\phi$ are the maximum control-field amplitude, angle of controlled z axis rotation, control-field fluence, gate distance, and gate robustness, respectively, in the corresponding scaled units described in Sec. II C.

Target operation: $Z_{\pi/2}$						
ε_0	0	1	2	3	4	5
$\max\|C_o\|$	2.4	18.5	18.4	18.3	6.7	5.9
$\theta(t_f;C_o)$	$\pi/2$	1.5779	1.6002	1.6406	−3.4333	−2.5660
$\Phi[C_o]$	3.4	84.5	83.0	80.7	17.5	12.1
$\Delta(Z_{\pi/2},U_{t_f})$	4.59×10^{-8}	1.11×10^{-7}	2.03×10^{-7}	6.23×10^{-8}	1.25×10^{-7}	3.94×10^{-8}
$\mathcal{R}_{\pi/2}[C_o,\varepsilon_0,0.5]$	7.40×10^{-2}	1.44×10^{-3}	3.65×10^{-3}	6.96×10^{-3}	5.04×10^{-2}	6.21×10^{-2}
Target operation: Z_π						
ε_0	0	1	2	3	4	5
$\max\|C_o\|$	4.8	12.2	12.1	11.9	11.6	11.4
$\theta(t_f;C_o)$	π	3.1020	2.9824	2.7802	2.4923	2.1181
$\Phi[C_o]$	13.7	39.5	38.4	36.5	34.1	31.4
$\Delta(Z_\pi,U_{t_f})$	6.05×10^{-8}	2.73×10^{-7}	3.16×10^{-8}	5.58×10^{-8}	4.34×10^{-8}	2.79×10^{-8}
$\mathcal{R}_\pi[C_o,\varepsilon_0,0.5]$	3.80×10^{-2}	6.95×10^{-3}	1.38×10^{-2}	2.05×10^{-2}	2.68×10^{-2}	3.24×10^{-2}

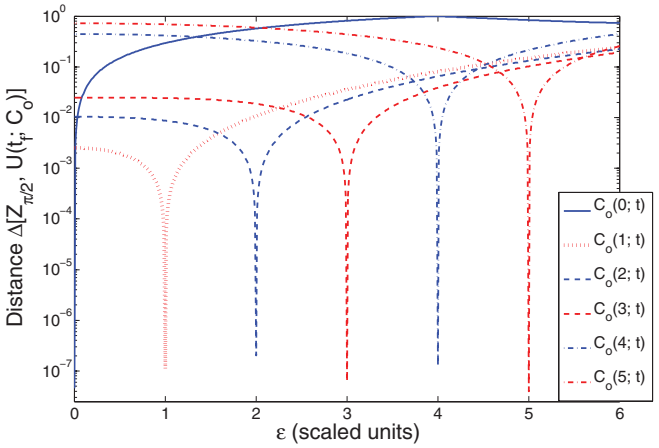

FIG. 3. (Color online) Distance of OCs optimized with *particular* values of epsilon, denoted as $C_o(\varepsilon_0;t)$, for the $Z_{\pi/2}$ operation $[\Delta(Z_{\pi/2},U_{t_f}) < 10^{-6}$ for all controls], subsequently applied over the interval $0 \leqslant \varepsilon \leqslant 6$ (with a resolution of 0.01 scaled units).

between OCs with shapes very similar to $C_o(3,t)$ and $C_o(4,t)$ reported in Fig. 1, corresponding to net positive and negative rotations, respectively. For the initial control field used in this work, this transition occurs when $\varepsilon_0 \approx 3.9$. Comparing the gate-distance responses in Fig. 3 for $C_o(3,t)$ and $C_o(4,t)$ reveals that these OCs are not equivalent solutions for unitary control; the difference between these controls is exclusively due to the effect of the different values of ε_0 on the qubit dynamics.

Quantum-computing architectures often assume encoded quantum operations to correct the inevitable errors due to control and environmental noise. Gate operations, such as Z_ϕ simulated here, must achieve a minimum fidelity threshold for successful quantum error correction. A predicted maximum distance Δ of less than 10^{-3} for $\varepsilon \in [0,5]$ is within typical ranges necessary for fault-tolerant QC [1,43,50]. These results highlight the potential advantage of using OCT if estimates of Hamiltonian parameters are known well. However, these OCs are not robust to uncertainty in the magnitude of ε; in fact, they

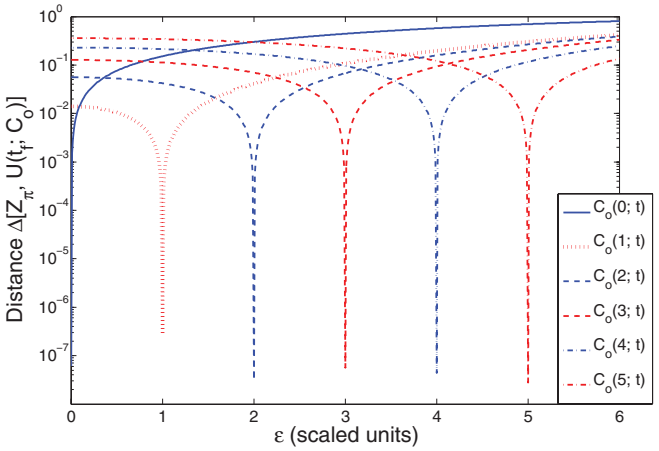

FIG. 4. (Color online) Distance of OCs optimized with *particular* values of epsilon, denoted as $C_o(\varepsilon_0;t)$, for the Z_π operation $[\Delta(Z_\pi,U_{t_f}) < 10^{-6}$ for all controls], subsequently applied over the interval $0 \leqslant \varepsilon \leqslant 6$ (with a resolution of 0.01 scaled units).

are highly sensitive to small perturbatives in ε. Uncertainty can result from incomplete or poor system parameter estimates as well as from dynamics of the environment [38,51].

The objective functional $\mathcal{J}$ in Eq. (6) does not include criteria to evaluate control-field robustness with respect to variations in ε. To investigate *any* inherent robustness quantitatively, OC fields optimized for particular values of ε [i.e., $C_o(\varepsilon_0;t)$] were subsequently applied to a surrounding interval of ε_0. Results are presented in Figs. 3 and 4 for the $Z_{\pi/2}$ and Z_π operations, respectively. Consider the distance response of $C_o(2;t)$ to variations in ε, which varies substantially with respect to variations that correspond to $\sim$1 mT fluctuations (corresponding to approximately $1.6 \leqslant \varepsilon \leqslant 2.4$) for GaAS DQD systems. Without specifying a measure of robustness as an additional control objective, the resulting OCs are not inherently robust to modest local magnetic-field fluctuations (e.g., at each quantum dot). Numerical calculations with these OCs for both operations indicate that the error in the measurement fidelity used to characterize ε for a particular system must be smaller than 10^{-2} (corresponding to approximately 1.3×10^{-5} or smaller T for the GaAs DQD example) to realize gates with distances that are 10^{-3} or smaller. Moreover, with these controls, ε could not drift significantly during a computation without serious fidelity loss.

In addition to the data presented in Figs. 3 and 4, we introduce the following functional to investigate robustness of Z_ϕ operations over the interval $[\varepsilon_-,\varepsilon_+]$:

$$\mathcal{R}_\phi[C,\varepsilon,\delta\varepsilon] := \int_{\varepsilon_-}^{\varepsilon_+} \Delta\left[Z_\phi,U_{t_f}(C)\right] d\varepsilon', \tag{13}$$

where $\varepsilon_\pm := \varepsilon \pm \delta\varepsilon$. Values for $\mathcal{R}_\phi[C_o,\varepsilon_0,0.5]$, corresponding to the average gate distance over a unit interval centered at ε_0, are reported in Table II. Quantifying robustness with this metric further demonstrates the general lack of robustness of these OCs; $\mathcal{R}_\phi$ varies from 1.44×10^{-3} (which is somewhat robust) to 7.40×10^{-2}.

V. ROBUST DECOUPLING-PULSE CRITERIA

Optimization of the functional $\mathcal{J}$ in Eq. (6) is highly underdetermined, and multiple control fields exist that will produce the same target operator V [59,66]. Requiring robustness to control and/or system variations involves the specification of additional constraints or penalties, such as Eq. (13), thereby limiting solutions to this OCT problem. In this section, we summarize a set of control-field constraints that characterize robustness to perturbative decoherence and adapt them to locate controls that are robust to system uncertainty.

A. General robustness criteria

Consider the following open-system Hamiltonian for one qubit:

$$H_{\text{open}}(t) := \vec{S}\cdot\vec{C}(t) + \vec{S}\cdot\vec{\Gamma} + H_e, \tag{14}$$

where $\vec{S} := (S_x,S_y,S_z)$ represents the spin-operator vector, $\vec{C}(t) := (C_x,C_y,C_z)$ represents a multipolarized control field, $\vec{\Gamma} := (\Gamma_x,\Gamma_y,\Gamma_z)$ represents the environment interaction operator, and H_e represents the environment Hamiltonian.

By expanding the final-time unitary evolution operator generated by H_{open} with respect to $t_f\|H_e\|$ and $t_f\|\vec{\Gamma}\|$ about $t_f\|H_e\| = 0$ and $t_f\|\vec{\Gamma}\| = 0$, Pasini *et al.* have identified control-field criteria necessary to eliminate perturbative first- and second-order effects resulting from the environment Hamiltonian H_e and the interaction term $\vec{S}\cdot\vec{\Gamma}$ [15]. Although applicable to multipolarized controls and general qubit-environment coupling, the methodology developed in this section assumes control-qubit coupling along the z axis and qubit-environment interaction along the x axis; namely,

$$H'_{\text{open}}(t) := C(t)S_z \otimes \mathbb{1}_{n_e} + S_x \otimes \Gamma_x + \mathbb{1}_2 \otimes H_e, \quad (15)$$

where $n_e := \dim\{\mathcal{H}_e\}$ and $\mathcal{H}_e$ is the Hilbert space of the environment. For controlled $\pi/2$ and π rotations about the z axis, Pasini *et al.* derived the following vector functional characterizing the space of controls that suppress first- and second-order effects errors resulting from an x axis interaction with the environment:

$$\vec{\zeta}[\theta] := (\zeta_1,\zeta_2,\zeta_3,\zeta_4,\zeta_5)^{\mathrm{T}}, \quad (16a)$$

where

$$\zeta_1[\theta] := \int_0^{t_f} \sin[\theta(t)]dt, \quad (16b)$$

$$\zeta_2[\theta] := \int_0^{t_f} \cos[\theta(t)]dt, \quad (16c)$$

$$\zeta_3[\theta] := \int_0^{t_f}\int_0^{t_f} \sin[\theta(t_1)-\theta(t_2)]\mathrm{sgn}(t_1-t_2)dt_1dt_2, \quad (16d)$$

$$\zeta_4[\theta] := \int_0^{t_f} t\sin[\theta(t)]dt, \quad (16e)$$

$$\zeta_5[\theta] := \int_0^{t_f} t\cos[\theta(t)]dt. \quad (16f)$$

Recall $\theta(t;C)$ from Eq. (8a) in Sec. III B, which represents the net rotation performed by the control field C during the time interval $[0,t]$.

For convenience and simplicity in the analysis that follows this section, we define $\vec{\eta}$ as

$$\vec{\eta}[C] := (\eta_1,\eta_2,\eta_3,\eta_4,\eta_5)^{\mathrm{T}}, \quad (17a)$$

where

$$\eta_i := \zeta_i \circ \theta. \quad (17b)$$

Thus, $\vec{\eta} : \mathfrak{C}_{t_f} \mapsto \mathbb{R}^5$. For one qubit, the components of $\vec{\eta}$ represent the first- and second-order perturbative errors, with respect to the final time t_f and error Hamiltonians Γ_x and H_e, of a controlled $\pi/2$ or π rotation about the z axis. Specifically, η_1 and η_2 represent first-order errors, while η_3, η_4, and η_5 represent second-order errors. Thus, when $\vec{\eta} = 0$, the pulse is accurate up to third-order, eliminating the first- and second-order effects resulting from a perturbative qubit-environment interaction. According to the analysis in Ref. [15], when $[H_e,\Gamma_\lambda] = 0$, for all λ, components η_4 and η_5 can be neglected from the vector constraint.

B. Closed-system robustness criteria

To apply these results to a closed one-qubit system and construct robust Z_ϕ operations for the DQD logical qubit using this criteria, we first compare the Hamiltonians H in Eq. (1) and H'_{open} in Eq. (15). These Hamiltonians are equal if $\Gamma_x = \varepsilon$ and $H_e = 0$, which implies that $[H_e,\Gamma_\lambda] = 0$, so $\vec{\eta}^{\,\mathrm{r}} := (\eta_1,\eta_2,\eta_3)^{\mathrm{T}}$ is the relevant *reduced* vector constraint. Incorporating these nonlinear equality constraints into the original optimization problem yields the following nonlinearly constrained control problem:

$$\min_{C\in\mathfrak{C}_{t_f}} \mathcal{J}[C] \quad \text{subject to } \vec{\eta}^{\,\mathrm{r}}[C] = 0. \quad (18)$$

Methods such as "diffeomorphic modulation under observable-response–preserving homotopy" (DMORPH) [58, 67–69] or sequential quadratic programming [70] are required to generate OCs that maintain or satisfy approximate feasibility, determined by $\vec{\eta}^{\,\mathrm{r}} = 0$. A technique using DMORPH is developed and applied in the next sections.

For a qubit described by the Hamiltonian in Eq. (1), control fields from Ref. [15] satisfying $\|\vec{\eta}^{\,\mathrm{r}}\|_2 < 10^{-7}$ (where $\|\cdot\|_2$ denotes the vector two norm) and corresponding gate distances for $\pi/2$ and π pulses are presented in Figs. 5 and 6, respectively. These fields are denoted as $C_{\mathrm{d}}(t)$, where the subscript "d" indicates the decoupling feature of these DPs. Satisfying the control-field constraints specified by Pasini *et al.* [15], first- and second-order perturbations about $\varepsilon = 0$ are eliminated. As such, gate distance increases with the magnitude of ε and optimum performance occurs when $\varepsilon = 0$, which is not necessarily expected to be valid for realistic qubit systems with drift terms (see, e.g., [45]). Although we use $\vec{\eta}^{\,\mathrm{r}} = 0$ as a general condition for robustness in this work, whether controls satisfying $\vec{\eta}^{\,\mathrm{r}} = 0$ are robust about points where $\varepsilon \neq 0$ remains an open question. However, comparing the gate distances in Fig. 6 to those in Figs. 3 and 4 reveals a certain degree of robustness in control fields $C_{\mathrm{d}}(t)$ relative to $C_{\mathrm{o}}(\varepsilon;t)$; for example, for both Z_ϕ operations and all values of ε_0 considered, $d\Delta/d\varepsilon$ around ε_0 for $C_{\mathrm{d}}(t)$ is much smaller than $C_{\mathrm{o}}(\varepsilon_0;t)$. Table III contains information about some of the properties of the DPs in Figs. 5 and 6.

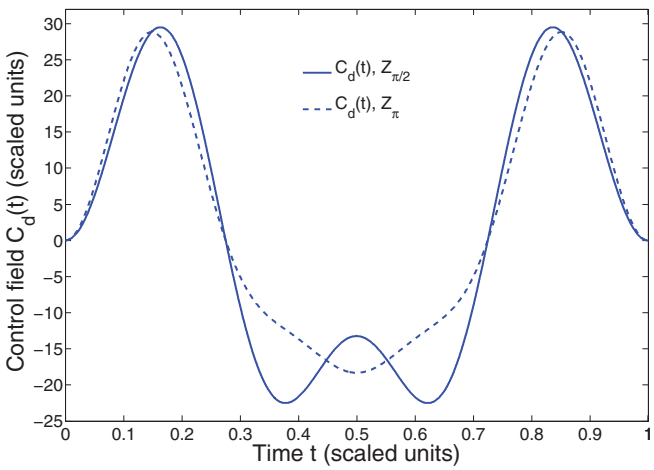

FIG. 5. (Color online) Control fields satisfying the DPC in Eq. (17), denoted as $C_{\mathrm{d}}(t)$, for Z_ϕ operations ($\|\vec{\eta}^{\,\mathrm{r}}\|_2 < 10^{-7}$), from Pasini *et al.* [15].

TABLE III. Performance of the DPs $C_{\rm d}(t)$ for one-qubit Z_ϕ operations. Here, Δ, $\mathcal{R}_\phi$, $\max|C_{\rm d}|$, θ, $\Phi[C] := \int_0^{t_{\rm f}} C^2(\varepsilon_0;t)dt$, and $\|\vec{\eta}^{\rm r}\|_2$ are the gate distance, gate robustness, maximum control-field amplitude, angle of controlled z axis rotation, control-field fluence, and constraint vector norm, respectively, in the corresponding scaled units described in Sec. II C.

Target operation: $Z_{\pi/2}$						
ε_0	0	1	2	3	4	5
$\Delta(Z_{\pi/2},U_{t_{\rm f}})$	7.60×10^{-8}	1.52×10^{-4}	1.34×10^{-3}	4.47×10^{-3}	1.02×10^{-2}	1.89×10^{-2}
$\mathcal{R}_{\pi/2}[C_{\rm d},\varepsilon_0,0.5]$	2.84×10^{-6}	1.96×10^{-4}	1.42×10^{-3}	4.58×10^{-3}	1.03×10^{-2}	1.91×10^{-2}
$\max\|C_{\rm d}\| = 29.5$, $\theta(t_{\rm f};C_{\rm d}) = \pi/2$, $\Phi[C_{\rm d}] = 335.5$, $\|\vec{\eta}^{\rm r}(t;C_{\rm d})\|_2 = 2.52\times10^{-8}$						
Target operation: Z_π						
ε_0	0	1	2	3	4	5
$\Delta(Z_\pi,U_{t_{\rm f}})$	5.67×10^{-8}	5.84×10^{-4}	4.63×10^{-3}	1.54×10^{-2}	3.56×10^{-2}	6.75×10^{-2}
$\mathcal{R}_\pi[C_{\rm d},\varepsilon_0,0.5]$	1.83×10^{-5}	7.29×10^{-4}	4.91×10^{-3}	1.58×10^{-2}	3.61×10^{-2}	6.81×10^{-2}
$\max\|C_{\rm d}\| = 28.8$, $\theta(t_{\rm f};C_{\rm d}) = \pi$, $\Phi[C_{\rm d}] = 264.8$, $\|\vec{\eta}^{\rm r}(t;C_{\rm d})\|_2 = 8.04\times10^{-8}$						

VI. HYBRID QUANTUM CONTROL: DECOUPLING-PULSE CRITERIA + OPTIMAL CONTROL THEORY

Given the favorable structure of quantum-control landscapes (e.g., trap-free structure, continua corresponding to optimal solutions, etc.) for regular controls [59,65,66,71], DMORPH provides a mathematical means to explore families of controls that achieve the same objective [58,67]. Applications of DMORPH include the continuous variation of a Hamiltonian while preserving or optimizing the value of a quantum mechanical observable [67,72] and exploring the level sets of state and unitary control [58,69,73]. DMORPH can also be used as direct optimization technique [74]. We develop DMORPH techniques to explore the space of controls corresponding to $\vec{\eta} = 0$ while optimizing $\mathcal{J}$ for a specified ε_0.

Expressed more formally, in this section, we develop a method to optimize $\mathcal{J}$ over the set $\mathfrak{C}^{\eta}_{t_{\rm f}} := \vec{\eta}^{\,-1}(0) \subset \mathfrak{C}_{t_{\rm f}}$; that is, the set of feasible controls satisfying $\vec{\eta} = 0$, where $\vec{\eta}^{\,-1}$ denotes the pre-image of $\vec{\eta}$.[1] To increase general applicability, we develop this technique for $\vec{\eta}$, rather than the reduced constraint $\vec{\eta}^{\rm r}$. Away from critical points of $\vec{\eta}$ (a real-valued vector); that is, controls for which the set of gradients $\{\nabla\eta_i\}$ are linearly dependent [75], $\mathfrak{C}^{\eta}_{t_{\rm f}}$ is a codimension-5 submanifold of $\mathfrak{C}_{t_{\rm f}}$ [76]. It is assumed that critical points of $\vec{\eta}$ are rare; an assumption supported by the success of the resulting algorithm. The gradient of the restricted functional $\mathcal{K} := \mathcal{J}|_{\mathfrak{C}^{\eta}_{t_{\rm f}}}$ at a point $C \in \mathfrak{C}^{\eta}_{t_{\rm f}}$ is just the projection of the gradient of $\mathcal{J}$ at C onto the tangent space $\mathrm{T}_C\mathfrak{C}^{\eta}_{t_{\rm f}}$ of $\mathfrak{C}^{\eta}_{t_{\rm f}}$ at C [58,77,78]. By systematically updating the control field iteratively using a GrA with this projected gradient, the algorithm is able to simultaneously improve the value of $\mathcal{J}$ and maintain approximate feasibility, or at least impede deviations from feasibility. It is unlikely that the quantum-control landscape for the restricted objective functional $\mathcal{K}$ is trap free. As such, a global optimization algorithm *might* be better suited to finding solutions. However, because a global parametrization of the set $\mathfrak{C}^{\eta}_{t_{\rm f}}$ is lacking, maintaining (approximate) feasibility (i.e., $\vec{\eta} = 0$) might be difficult in general.

[1] The pre-image of a particular subset $S \subset Y$ of the codomain of a function $f : X \mapsto Y$ is the set of all elements of the domain X of f that map to elements of S [i.e., $f^{-1}(S) := \{x \in X : f(x) \in S\}$]. Because $\vec{\eta} : \mathfrak{C}_{t_{\rm f}} \mapsto \mathbb{R}^5$, this implies that $\vec{\eta}^{\,-1} : \mathbb{R}^5 \mapsto \mathfrak{C}_{t_{\rm f}}$.

A. Gradients of feasibility constraints

Using DMORPH to remove the components of $\nabla\mathcal{J}$ that cause a change in $\vec{\eta}$ requires the gradient of each element of $\vec{\eta}$, $\nabla\eta_i$:

$$(\nabla\eta_i[C])(t) = \int_0^{t_{\rm f}} \frac{\delta\zeta_i[\theta]}{\delta\theta(\tau)}\frac{\delta\theta(\tau)}{\delta C(t)}d\tau = \int_t^{t_{\rm f}} \frac{\delta\zeta_i[\theta]}{\delta\theta(\tau)}d\tau \tag{19a}$$

$$\Rightarrow \begin{pmatrix}(\nabla\eta_1[C])(t)\\ \vdots \\ (\nabla\eta_5[C])(t)\end{pmatrix} = \begin{pmatrix} \int_t^{t_{\rm f}} \cos[\theta(\tau)]d\tau \\ \int_t^{t_{\rm f}} \sin[\theta(\tau)]d\tau \\ 2\int_t^{t_{\rm f}}\int_0^{t_{\rm f}} \{\cos[\theta(\tau)]\cos[\theta(\tau')] + \sin[\theta(\tau)]\sin[\theta(\tau')]\}\mathrm{sgn}(\tau-\tau')d\tau' d\tau \\ \int_t^{t_{\rm f}} \tau\cos[\theta(\tau)]d\tau \\ \int_t^{t_{\rm f}} \tau\sin[\theta(\tau)]d\tau \end{pmatrix}. \tag{19b}$$

As expressed here, the vector of gradients $\nabla\eta_i$ is a function of the time variable t. Note that the set $\{\nabla\eta_i\}$ spans the normal space $(\mathrm{T}_C\mathfrak{C}^{\eta}_{t_\mathrm{f}})^{\perp}$ when $C \in \mathfrak{C}^{\eta}_{t_\mathrm{f}}$ is a regular point of $\vec{\eta}$.

B. Gradient projection method

In addition to the gradients $\nabla\eta_i$, we also need a vector that specifies the relative weight of each gradient component to remove. This is determined by first calculating the Gramian matrix, with elements

$$(G_c)_{ij} := \langle \nabla\eta_i[C], \nabla\eta_j[C] \rangle_{\mathfrak{C}_{t_\mathrm{f}}} . \tag{20}$$

In general, G_c is not guaranteed to be full rank; nonsingularity of G_c must be explored (numerically) as a function of C. The Gramian matrix G_c is rank deficient if and only if elements in the set $\{\nabla\eta_i\}$ are linearly dependent (i.e., if and only if C is a critical point of $\vec{\eta}$ [75]). However, when $\nabla\eta_i$ are all linearly independent, G_c is invertible. With Eqs. (19) and (20), all gradient directions $\nabla\eta_i$ can be removed from $\nabla\mathcal{J}$, producing $\nabla\mathcal{K}$ as follows:

$$\nabla\mathcal{K}[C] = \nabla\mathcal{J}[C] - \sum_{i=1}^{5} \nabla\eta_i[C] \left\{ G_c^{-1} \left[\vec{q}_c \left(\nabla\mathcal{J}[C] \right) \right] \right\}_i , \tag{21a}$$

where $\mathcal{K} : \mathfrak{C}^{\eta}_{t_\mathrm{f}} \to \mathbb{R}$ is a restriction of $\mathcal{J}$ (i.e., $\mathcal{K} := \mathcal{J}|_{\mathfrak{C}^{\eta}_{t_\mathrm{f}}}$) and $\vec{q}_c$ has elements

$$[\vec{q}_c(\nabla\mathcal{J}[C])]_i := \langle \nabla\mathcal{J}[C], \nabla\eta_i[C] \rangle_{\mathfrak{C}_{t_\mathrm{f}}} . \tag{21b}$$

Thus, $\nabla\mathcal{K}$ is a vector field on $\mathfrak{C}^{\eta}_{t_\mathrm{f}}$, and the ordinary differential equation (ODE)

$$\frac{dC(s)}{ds} = -\nabla\mathcal{K}[C(s)] \tag{22}$$

describes the gradient flow of $\mathcal{K}$ on $\mathfrak{C}^{\eta}_{t_\mathrm{f}}$ that minimizes $\mathcal{J}$ without changing the value of $\vec{\eta}$. The GrA in this work implements a forward Euler integration of this equation, which should be sufficiently accurate, provided that the multiplier β in Eq. (11) is selected properly; that is, β is within the validity of the linear approximation of the tangent space at C. Higher-order numerical ODE solvers (e.g., Runge-Kutta methods [63]) might offer higher accuracy and/or greater efficiency but have not been explored in this work.

Equation (21) describes the orthogonal projection from $\mathrm{T}_C\mathfrak{C}_{t_\mathrm{f}}$ to $\mathrm{T}_C\mathfrak{C}^{\eta}_{t_\mathrm{f}}$. That $\nabla\mathcal{K}$ is orthogonal to all elements of $\{\nabla\eta_i\}$ can be verified as follows: Let

$$\xi := \sum_{i=1}^{5} \chi_i \nabla\eta_i[C]; \tag{23}$$

that is, ξ is a linear combination of the elements of the set $\{\nabla\eta_i\}$, where $\chi_i \in \mathbb{R}$. Replacing $\nabla\mathcal{J}$ with ξ in Eq. (21) yields

$$\begin{aligned} &\xi - \sum_{i=1}^{5} \nabla\eta_i[C] \left\{ G_c^{-1}[\vec{q}_c(\xi)] \right\}_i \\ &\quad = \xi - \sum_{i=1}^{5} \nabla\eta_i[C] \left(G_c^{-1} G_c \vec{\chi} \right)_i = 0, \end{aligned} \tag{24}$$

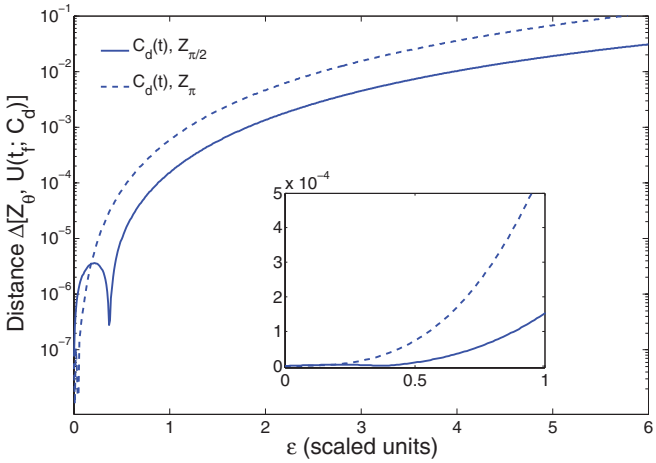

FIG. 6. (Color online) Distance of the Z_ϕ operations as a function of ε (with a resolution of 0.01 scaled units) and $\phi \in \{\pi/2, \pi\}$ for the Landau-Zener model of Eq. (1) and control fields $C_\mathrm{d}(t)$ presented in Fig. 5. The inset displays the gate distance for $0 \leqslant \varepsilon \leqslant 1$ in greater detail, on a linear scale.

where $\vec{\chi} := (\chi_1, \chi_2, \chi_3, \chi_4, \chi_5)^{\mathrm{T}}$. If $\xi \in \mathrm{T}_C\mathfrak{C}_{t_\mathrm{f}}$ is such that ξ is orthogonal to all gradients $\nabla\eta_i$, then the projection described in Eq. (21) acts as identity on ξ. Together with the previous statement, this shows that Eq. (21) is the orthogonal projector from $\mathrm{T}_C\mathfrak{C}_{t_\mathrm{f}}$ to $\mathrm{T}_C\mathfrak{C}^{\eta}_{t_\mathrm{f}}$.

As mentioned in the introduction, because we combine DPC and OCT methods to generate improved control fields, we denote the integrated optimization procedure described in this section as DPC + OCT. Straightforward modifications of G_c and $\vec{q}_c$ are required when $\vec{\eta}^{\,\mathrm{r}}$ is the constraint vector rather than $\vec{\eta}$ [i.e., $G_c \in \mathcal{M}_3(\mathbb{R})$ rather than $\mathcal{M}_5(\mathbb{R})$], and $\vec{q}_c(\nabla\mathcal{J}) \in \mathbb{R}^3$ rather than $\mathbb{R}^5$.

VII. RESULTS FROM DECOUPLING-PULSE CRITERIA + OPTIMAL CONTROL THEORY

Using the DPC + OCT protocol described in Sec. VI and the DPs in Fig. 5 for the initial iterations of all values of ε_0 considered, we sought to numerically explore the space of controls satisfying $\vec{\eta}^{\,\mathrm{r}} = 0$ and $\Delta = 0$ to improve control fidelity *and* robustness to ε uncertainty for $Z_{\pi/2}$ and Z_π operations, compared to the original DPs. To a certain extent, it appears *a priori* that the minimization of Δ and $\vec{\eta}^{\,\mathrm{r}}$ might be competing control objectives. For example, compare the gate-distance plots for OCT (Figs. 3 and 4) to those for the DPs (Fig. 6) over the interval $0 \leqslant \varepsilon \leqslant 6$ (with a numerical resolution of 0.01 scaled units). OCT for the design of unitary operations, as we have formulated it in Sec. III, seeks to minimize Δ for a *particular* value of ε; namely, the parameter estimate ε_0. Because the system described by the Hamiltonian in Eq. (1) is controllable and the underlying control landscape possesses a fortuitous structure for regular controls [59,66], a GrA achieves this objective quite efficiently and successfully. However, as presented in Sec. IV, these OCs are not inherently robust to perturbations in ε, whereas controls satisfying $\vec{\eta}^{\,\mathrm{r}} = 0$ are nearly optimal (with respect to $\mathcal{J}$) when $\varepsilon_0 \approx 0$. This scenario illustrates the potential balance that can exist between fidelity and robustness in general.

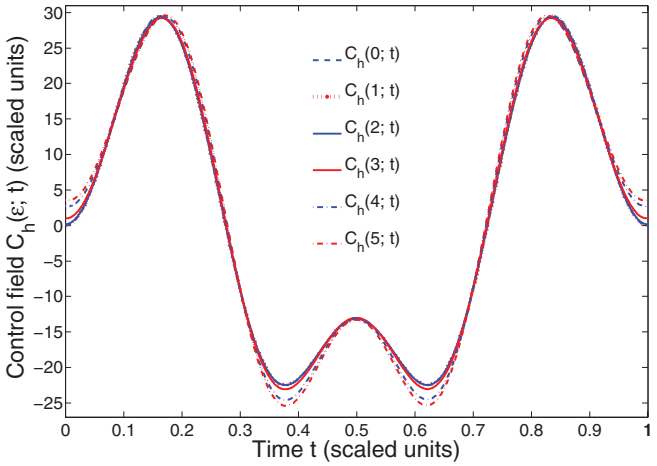

FIG. 7. (Color online) DPC + OCT fields $C_{\rm h}(\varepsilon_0;t)$ producing a $Z_{\pi/2}$ operation, optimized using $C_{\rm d}(t)$ as the initial control for all estimates/values of ε_0 and $t_{\rm f}=1$ scaled unit. Although distinct, note that $C_{\rm h}(0;t)$, $C_{\rm h}(1;t)$, and $C_{\rm h}(2;t)$ appear nearly indistinguishable in this figure.

Overall, the controls that satisfy $\vec{\eta}^{\,\rm r}=0$ are reasonably robust to perturbations in ε, provided that ε and/or $\Delta\varepsilon$ are within the perturbative limit. Given that these two control objectives are potentially competing, we use the hybrid optimization procedure developed in Sec. VI to suppress deviations from $\vec{\eta}^{\,\rm r}=0$ but not entirely eliminate them. In other words, convergence of the DMORPH DPC + OCT algorithm occurs only when $\mathcal{J}$ stops decreasing, not when $\vec{\eta}^{\,\rm r}$ starts increasing.

Because the formulation of OCT requires the specification of ε, we consider $\varepsilon_0\in[0,5]$. As before, the final time for all controls was fixed at $t_{\rm f}=1$ scaled unit of time. DPC + OCT fields for $Z_{\pi/2}$ and Z_π are presented in Figs. 7 and 8, respectively. These fields are denoted as $C_{\rm h}(\varepsilon_0;t)$, where the subscript "h" indicates the hybrid feature of this QCP. Corresponding results for the gate distance Δ are presented in Figs. 9 and 10; results for the vector-constraint norm $\|\vec{\eta}^{\,\rm r}\|_2$ and objective functional $\mathcal{J}$ are presented in Figs. 11 and 12.

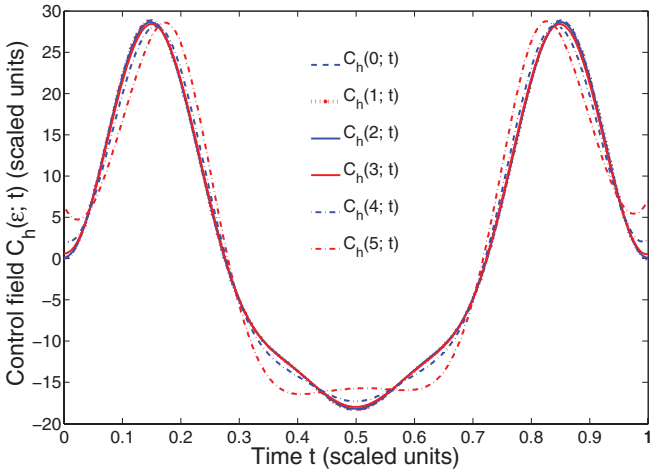

FIG. 8. (Color online) DPC + OCT fields $C_{\rm h}(\varepsilon_0;t)$ producing a Z_π operation, optimized using $C_{\rm d}(t)$ as the initial control for all values of ε_0 and $t_{\rm f}=1$ scaled unit. Although distinct, note that $C_{\rm h}(0;t)$, $C_{\rm h}(1;t)$, and $C_{\rm h}(2;t)$ appear nearly indistinguishable in this figure.

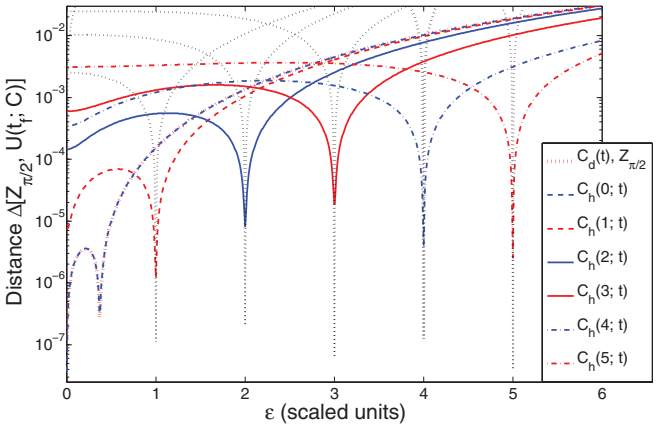

FIG. 9. (Color online) Distance for the $Z_{\pi/2}$ operation as a function of ε (with a resolution of 0.01 scaled units) for control fields satisfying (a) $\vec{\eta}^{\,\rm r}=0$ [red dashed line, which is very similar to that for $C_{\rm h}(0;t)$], (b) $\vec{\eta}^{\,\rm r}\approx 0$ and $\Delta\approx 0$, optimized with a *specified* value of ε_0, and (c) results from $C_{\rm o}(\varepsilon_0;t)$ in Sec. IV (black dashed lines, from Fig. 3).

In addition, Table IV contains information about some of the properties of the DPC + OCT fields. For both Z_ϕ operations, when $\varepsilon_0\geqslant 2$, we note that $\|\vec{\eta}^{\,\rm r}\|_2>10^{-4}$. However, since the robustness criteria quantified by $\vec{\eta}^{\,\rm r}$ were obtained from a perturbative analysis about $\varepsilon_0=0$, it remains an open question whether, *a priori*, control fields satisfying $\vec{\eta}^{\,\rm r}=0$ for $\varepsilon_0>0$ will be robust to fluctuations about ε_0. However, as we present in this section, control solutions obtained from the DPC + OCT protocol have some desirable properties, even when $\varepsilon_0>0$. It is interesting to explore the results of the DPC + OCT protocol when the distance is relatively large (i.e., $\Delta>10^{-3}$) and the sensitivity to changes in ε is small (e.g., as illustrated in Fig. 6).

Despite their unique gate-distance dependence of these control solutions on ε, as shown in Figs. 9 and 10 over the interval $0\leqslant\varepsilon\leqslant 6$ (with a numerical resolution of 0.01 scaled

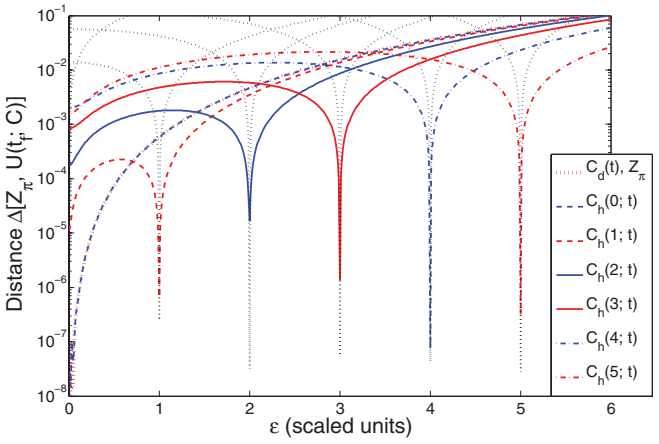

FIG. 10. (Color online) Distance for the Z_π operation as a function of ε (with a resolution of 0.01 scaled units) for control fields satisfying (a) $\vec{\eta}^{\,\rm r}=0$ [red dashed line, which is very similar to that for $C_{\rm h}(0;t)$], (b) $\vec{\eta}^{\,\rm r}\approx 0$ and $\Delta\approx 0$, optimized with a *specified* value of ε_0, and (c) results from $C_{\rm o}(\varepsilon_0;t)$ in Sec. IV (black dashed lines, from Fig. 4).

TABLE IV. Performance of the DPC + OCT controls $C_{\rm h}(\epsilon_0;t)$ for one-qubit Z_ϕ operations. Here, $\max|C_{\rm h}|$, θ, $\Phi[C]:=\int_0^{t_{\rm f}} C^2(\varepsilon_0;t)dt$, Δ, $\|\vec{\eta}^{\,\rm r}\|_2$, and $\mathcal{R}_\phi$ are the maximum control-field amplitude, angle of controlled z axis rotation, control-field fluence, gate distance, constraint vector norm, and gate robustness, respectively, in the corresponding scaled units described in Sec. II C.

Target operation: $Z_{\pi/2}$						
ε_0	0	1	2	3	4	5
$\max\|C_{\rm h}\|$	29.5	29.5	29.3	29.2	29.4	29.6
$\theta(t_{\rm f};C_{\rm h})$	$\pi/2$	$\pi/2$	1.5704	1.5690	1.5695	1.5792
$\Phi[C_{\rm h}]$	335.5	334.6	332.8	337.4	356.5	370.5
$\Delta(Z_{\pi/2},U_{\rm f})$	3.65×10^{-8}	1.21×10^{-6}	8.23×10^{-6}	1.86×10^{-5}	4.08×10^{-6}	2.55×10^{-6}
$\|\vec{\eta}^{\,\rm r}(t_{\rm f};C_{\rm h})\|_2$	3.21×10^{-8}	4.74×10^{-4}	2.13×10^{-3}	4.21×10^{-3}	4.12×10^{-3}	2.45×10^{-3}
$\mathcal{R}_{\pi/2}[C_{\rm h},\varepsilon_0,0.5]$	2.84×10^{-6}	9.47×10^{-5}	3.55×10^{-4}	6.46×10^{-4}	5.72×10^{-4}	9.20×10^{-4}
Target operation: Z_π						
ε_0	0	1	2	3	4	5
$\max\|C_{\rm h}\|$	28.8	28.8	28.6	28.4	28.4	28.9
$\theta(t_{\rm f};C_{\rm h})$	π	π	3.1411	3.1392	3.1343	3.1320
$\Phi[C_{\rm h}]$	264.8	264.0	261.8	259.1	260.0	280.7
$\Delta(Z_\pi,U_{\rm f})$	2.36×10^{-8}	6.57×10^{-7}	1.67×10^{-5}	1.74×10^{-5}	2.79×10^{-8}	1.10×10^{-6}
$\|\vec{\eta}^{\,\rm r}(t_{\rm f};C_{\rm h})\|_2$	3.55×10^{-9}	9.93×10^{-5}	4.90×10^{-4}	1.10×10^{-3}	6.49×10^{-3}	2.10×10^{-2}
$\mathcal{R}_\phi[C_{\rm h},\varepsilon_0,0.5]$	1.83×10^{-5}	3.11×10^{-4}	1.18×10^{-3}	2.59×10^{-3}	4.23×10^{-3}	4.92×10^{-3}

units), the converged DPC + OCT fields for $\varepsilon_0\in\{0,1,2,3\}$ are very similar to each other and the originated DP for each target unitary operation. This supports the observation in Sec. IV that this simple system can effectively discriminate between very similar control fields [i.e., as measured by the gate distance Δ in Eq. (4)], the qubit system is quite sensitive to these relatively small control-field variations. For example, although $\max_t\|C_{\rm h}(1;t)-C_{\rm h}(2;t)\|<0.2$ scaled units of energy for both operations, and the mean relative difference is approximately 1.5% and 1.3% for the $Z_{\pi/2}$ and Z_π operations, respectively, the corresponding gate distances (presented in Figs. 9 and 10) do not coincide significantly when $0\leqslant\varepsilon\leqslant3$.

Interestingly, the DPC + OCT control field for the Z_π operation when $\varepsilon_0=5$ has some distinguishing features compared to the fields for the other values of ε_0. Based on the relatively large distance Δ of the corresponding $C_{\rm d}(t)$ control used for the initial iterate in the DPC + OCT protocol ($\Delta=6.75\times10^{-2}$), this value of ε_0 is not within the perturbative limit of the analysis that produced the vector constraint $\vec{\eta}^{\,\rm r}=0$. With such a large distance at $\varepsilon_0=5$, the DPC + OCT routine improves the distance by a factor larger than 10^4 and simultaneously improves the robustness $\mathcal{R}_\pi$ for $4.5\leqslant\varepsilon\leqslant5.5$ by a factor larger than 10, compared to the corresponding results for $C_{\rm d}(t)$ presented in Table III.

Figures 9 and 10 compare the distance of $C_{\rm d}(t)$ and $C_{\rm h}(\varepsilon_0;t)$ control fields for both Z_ϕ operations. Compared to $C_{\rm d}(t)$, all control fields $C_{\rm h}(\varepsilon_0;t)$ for $\varepsilon_0\geqslant0$ exhibit improved robustness to ε uncertainties in an interval around the nominal value ε_0 used in the DPC + OCT algorithm. This result demonstrates the utility of combining so-called "predesign" methods, which are based on mathematically analyzing general models [e.g., Eq. (14)], such as the DPC developed by Pasini *et al.* [15], with numerical OCT procedures and simple estimates of system

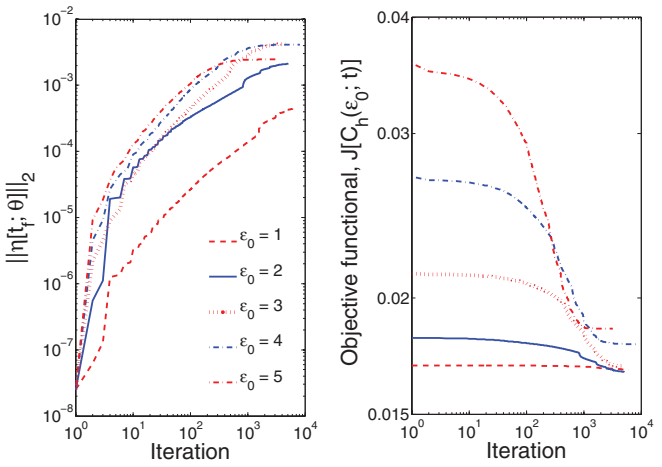

FIG. 11. (Color online) $\|\vec{\eta}^{\,\rm r}\|_2$ and objective functional $\mathcal{J}$ for the $Z_{\pi/2}$ operation and each value of ε_0 considered, as a function of the number of DPC + OCT algorithm iterations.

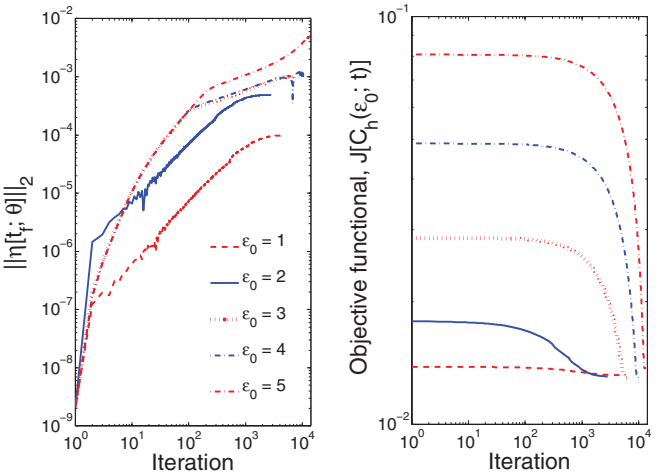

FIG. 12. (Color online) $\|\vec{\eta}^{\,\rm r}\|_2$ and objective functional $\mathcal{J}$ for the Z_π operation and each value of ε_0 considered, as a function of the number of DPC + OCT algorithm iterations.

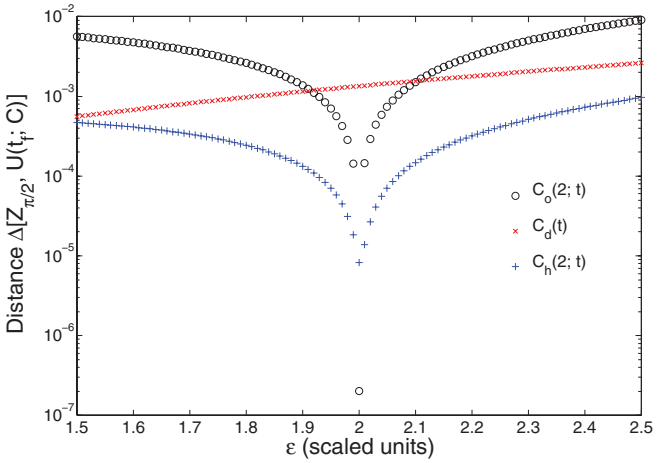

FIG. 13. (Color online) Distance for the $Z_{\pi/2}$ operation as a function of ε for $C_{\rm o}(2;t)$, $C_{\rm d}(t)$, and $C_{\rm h}(2;t)$ controls in a unit interval centered at $\varepsilon_0 = 2$ (with a resolution of 0.01 scaled units). Note that for $\varepsilon \geqslant 0.7$, $\Delta[Z_\pi, U(t_{\rm f}; C_{\rm d})] \geqslant \Delta[Z_\pi, U(t_{\rm f}; C_{\rm h})]$; that is, $C_{\rm h}(1;t)$ outperforms $C_{\rm d}(t)$.

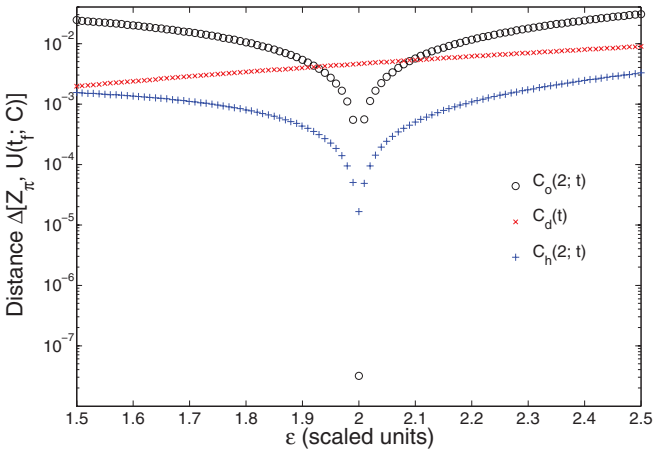

FIG. 14. (Color online) Distance for the Z_π operation as a function of ε for $C_{\rm o}(2;t)$, $C_{\rm d}(t)$, and $C_{\rm h}(2;t)$ controls in a unit interval centered at $\varepsilon_0 = 2$ (with a resolution of 0.01 scaled units). Note that for $\varepsilon \geqslant 1.5$, $\Delta[Z_\pi, U(t_{\rm f}; C_{\rm d})] \geqslant \Delta[Z_\pi, U(t_{\rm f}; C_{\rm h})]$; that is, $C_{\rm h}(1;t)$ outperforms $C_{\rm d}(t)$.

parameters (e.g., estimates of ε_0), especially when capabilities for shaping control fields are available. By combining these QCPs, we have developed a form of hybrid quantum control; estimates of system parameters can be directly incorporated into simulations to generate improved quantum operations for information processing and memory.

Figures 11 and 12 compare the vector-constraint norm $\|\vec{\eta}^{\,\rm r}\|_2$ and objective functional $\mathcal{J}$ as a function of the optimization iteration for both Z_ϕ operations. Overall, $\|\vec{\eta}^{\,\rm r}\|_2$ increases as $\mathcal{J}$ decreases, which is consistent with the notion of minimizing $\|\vec{\eta}^{\,\rm r}\|_2$ and $\mathcal{J}$ as potentially competing control objectives. Even though components of $\nabla\mathcal{J}$ that are parallel to all gradients $\nabla\eta_i$ are removed at each iteration, $\|\vec{\eta}^{\,\rm r}\|_2$ increases during the optimization for (at least) two reasons: (a) Eq. (21) removes components of $\nabla\eta_i$ (where elements η_i are *nonlinear* functions of the control) using an iterative linear projection method and (b) convergence of the DPC + OCT routine does not depend on $\|\vec{\eta}^{\,\rm r}\|_2$.

To aid in the comparative analysis of results from OCT, DPC, and the DPC + OCT procedures, OC gate-distance data from Figs. 3 and 4 are also presented in Figs. 9 and 10, respectively. Although the OC fields $C_{\rm o}(\varepsilon_0;t)$ all outperform the DPC + OCT fields $C_{\rm h}(\varepsilon_0;t)$ at ε_0, these OCs do not have the robustness of the DPs or DPC + OCT fields. To emphasize this feature, Figs. 13 and 14 present $Z_{\pi/2}$ and Z_π gate distances for $C_{\rm o}(2;t)$, $C_{\rm d}(t)$, and $C_{\rm h}(2;t)$ controls over a unit interval centered at $\varepsilon_0 = 2$. For both gates, $C_{\rm o}(2;t)$ is very sensitive to variations in ε; for example, when ε changes from 2 to 2 ± 0.01 (a change corresponding to approximately 1.3×10^{-5} T for the GaAs DQD example), the $Z_{\pi/2}$ gate distance increases (approximately) from 10^{-7} to 10^{-4}, while the Z_π gate distance increases from 10^{-8} to 10^{-4}, approaching the fault-tolerant threshold. However, for $C_{\rm h}(2;t)$ for both gates, as ε varies from ε_0, the increase in gate distance is much more gradual. Figures 13 and 14 contain some useful information to help understand the benefit of the hybrid DPC + OCT protocol. By combining DPC, OCT, a DP that satisfies $\vec{\eta}^{\,\rm r} = 0$ for the initial GrA iteration, and an estimate of the value of ε_0, the gate distance is decreased compared to the gate distance of the original DP for the entire unit interval centered at ε_0. Depending on the uncertainty magnitude of ε, this benefit could yield a potentially substantial decrease in the required concatenation or encoding resources necessary for QECCs, which depend on gate errors.

As a final illustrative example, consider the Z_π operation applied to the initial state $|\sigma_x^+\rangle$, implemented with the corresponding controls $C_{\rm o}(2;t)$, $C_{\rm d}(t)$, and $C_{\rm h}(2;t)$, which are applied to an ensemble of systems described by the Hamiltonian in Eq. (1) and the interval $1.5 \leqslant \varepsilon \leqslant 2.5$ (numerically distributed over 20 equal increments of 0.05 scaled units). The target state is $|\sigma_x^-\rangle = Z_\pi|\sigma_x^+\rangle$, where $\sigma_x|\sigma_x^\pm\rangle = \pm|\sigma_x^\pm\rangle$, and the ensemble of final states for a given control is denoted by $\{|\psi_i\rangle\}$. This state-based example clarifies the gate improvement obtained from $C_{\rm h}(2;t)$, compared to $C_{\rm o}(2;t)$ and $C_{\rm d}(t)$. To quantify the fidelity of the controls, we use the Uhlmann state fidelity for pure states [79,80]:

$$\mathcal{F}_{\rm u}(|\psi_1\rangle,|\psi_2\rangle) := |\langle\psi_1|\psi_2\rangle|\,, \tag{25}$$

where $|\psi_1\rangle$ and $|\psi_2\rangle$ are normalized vectors in $\mathcal{H}$. For a given control, we denote the resulting minimum, maximum, and average state fidelity, and the standard deviation of the fidelity of the ensemble as $\min_{|\psi_i\rangle}\mathcal{F}_{\rm u}$, $\max_{|\psi_i\rangle}\mathcal{F}_{\rm u}$, $\bar{\mathcal{F}}_{\rm u}$, and $\sigma_{\mathcal{F}_{\rm u}}$, respectively, which are presented in Table V for $C_{\rm o}(2;t)$, $C_{\rm d}(t)$, and $C_{\rm h}(2;t)$. Comparing the respective quantities, $C_{\rm h}(2;t)$ has the largest average and minimum fidelity and the smallest standard deviation of fidelity of the ensemble (by nearly a factor of 10). The final-time ensembles are also illustrated in Fig. 15, which contains a plot of resulting final states for each control, along with the target state $|\sigma_x^-\rangle$, all in the Bloch vector coordinates y and z. Because $-1 \leqslant x < -0.995$ for all final states, it is not included in this figure. Unlike the Bloch vector components corresponding to the final states produced from $C_{\rm o}(2;t)$ and $C_{\rm d}(t)$, the Bloch vector components produced from $C_{\rm h}(2;t)$ are tightly distributed around the target state, with most of the error distributed uniformly along the z axis, centered at the target state $|\sigma_x^-\rangle$. Very similar results are

TABLE V. Properties of state fidelity for the transition $|\sigma_x^-\rangle = Z_\pi|\sigma_x^+\rangle$ driven by controls $C_o(2;t)$, $C_d(t)$, and $C_h(2;t)$. Here, $\min_{|\psi_i\rangle}\mathcal{F}_u$, $\max_{|\psi_i\rangle}\mathcal{F}_u$, $\bar{\mathcal{F}}_u$, and $\sigma_{\mathcal{F}_u}$ denote the minimum, maximum, and average fidelity and the standard deviation of the fidelity, respectively, of the ensemble of final states $\{|\psi_i\rangle\}$ compared to the target state $|\sigma_x^-\rangle$.

	Target state: $\|\sigma_x^-\rangle = Z_\pi\|\sigma_x^+\rangle$			
	$\min_{\|\psi_i\rangle}\mathcal{F}_u\left[\|\sigma_x^-\rangle,\|\psi_i\rangle\right]$	$\max_{\|\psi_i\rangle}\mathcal{F}_u\left[\|\sigma_x^-\rangle,\|\psi_i\rangle\right]$	$\bar{\mathcal{F}}_u$	$\sigma_{\mathcal{F}_u}$
$C_o(2;t)$	0.996197	1.0	0.998871	1.082×10^{-3}
$C_d(t)$	0.999678	0.999985	0.999884	9.398×10^{-5}
$C_h(2;t)$	0.999958	1.0	0.999991	1.129×10^{-5}

obtained for the $Z_{\pi/2}$ operation implemented with $C_o(2;t)$, $C_d(t)$, and $C_h(2;t)$, applied to an ensemble of systems where $1.5 \leqslant \varepsilon \leqslant 2.5$.

VIII. CONCLUSIONS AND FUTURE DIRECTIONS

Combining OCT with the DPC established by Pasini *et al.* introduces improvements to the control of quantum systems for information processing. Given a reasonable characterization of the angular frequency $\varepsilon/\hbar$ of a persistent, but somewhat uncertain rotation about the x axis, a near-optimal fidelity can be achieved for $\varepsilon \geqslant 0$. Furthermore, the resulting DPC + OCT controls exhibit improved robustness to uncertainty in ε, compared to the original DPs. The systematic integration of general DPC and control-field shaping methods from OCT, therefore, promises considerable improvement over DPC or OCT strategies alone. We have provided a quantitative illustration for a logical qubit based on a DQD system, with continuous controls that possess reasonable magnitudes [64], based on the scaled-to-SI unit mapping.

We are currently investigating the benefits of these DPC + OCT $\pi/2$ and π pulses for memory and information processing in the presence of a decohering spin bath. It will be useful to determine how these pulses extend spin echoes and improve general DD and dynamically corrected gate pulse sequences, such as those described in Refs. [3,4,17,81–85]. Future work involves an exploration of unitary control sensitivity to fluctuations in the control field itself (e.g., control noise). *Postfacto* analysis of both the OCT and DPC + OCT results presented in this article for the general qubit model suggests that these fluctuations may contribute just as significantly to gate errors as corresponding system and environment fluctuations. However, our optimization criteria does not include robustness to control-field noise; such robustness may be sacrificed in favor of the actual criteria. Given the ubiquity of noise in classical controls and quantum mechanical systems, constructing controls and systems that are robust to their own noise is crucial for practical fault-tolerant QC.

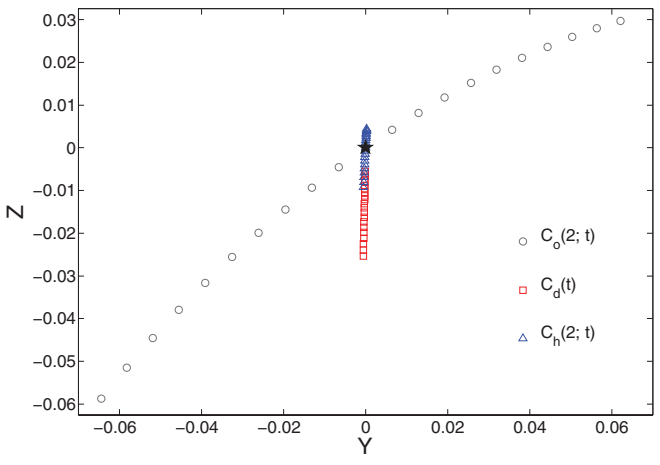

FIG. 15. (Color online) Final state in the Bloch vector coordinates y and z for the Z_π operation, implemented with the corresponding controls $C_o(2;t)$, $C_d(t)$, and $C_h(2;t)$ applied to an ensemble of systems described by the Hamiltonian in Eq. (1) and the interval $1.5 \leqslant \varepsilon \leqslant 2.5$ (distributed over 20 equal increments of 0.05 scaled units). The target state is $|\sigma_x^-\rangle = Z_\pi|\sigma_x^+\rangle$. Because $-1 \leqslant x < -0.995$ for all final states, it is not included in this figure.

Extensions of the original analysis by Pasini *et al.* are also being considered. We are interested in generalizing their results to include (a) arbitrary angle rotations and axes, (b) closed-system perturbative expansions about any value of ε, rather than only $\varepsilon = 0$, and (c) ε as a stochastic time-dependent variable or operator, which is relevant to previous research on decoherence control (see, e.g., [86]). In addition, direct minimization of $\mathcal{R}_\phi$ [Eq. (13)] or

$$\mathcal{L}[C] := \int_{\varepsilon_1}^{\varepsilon_2} \left(c_1 \left\| \frac{dU_{t_f}(C)}{d\varepsilon} \right\|_{HS} + c_2 \left\| \frac{d^2U_{t_f}(C)}{d\varepsilon^2} \right\|_{HS} \right) d\varepsilon \tag{26}$$

over $\mathcal{J}^{-1}(0)$, where $c_1, c_2 \in \mathbb{R}$ weight the relative significance of the two norms, are purely OCT means to improve robustness to variations in ε about any fixed interval $[\varepsilon_1,\varepsilon_2]$, which we are also investigating.

ACKNOWLEDGMENTS

M. D. G. thanks Paul T. Boggs (SNL-CA), and Robert L. Kosut (SC Solutions, Inc.) for illuminating discussions on control and nonlinear optimization. M. D. G. and W. M. W. thank Stefano Pasini and Götz S. Uhrig (Technische Universität Dortmund) for useful discussions regarding Ref. [15]. This work was supported by the Laboratory Directed Research and Development program at Sandia National Laboratories. Sandia is a multiprogram laboratory managed and operated by Sandia Corporation, a wholly owned subsidiary of Lockheed Martin Corporation, for the United States Department of Energy's National Nuclear Security Administration under contract DE-AC04-94AL85000.

[1] F. Gaitan, *Quantum Error Correction and Fault Tolerant Quantum Computing* (CRC Press, Boca Raton, FL, 2008).
[2] T. D. Ladd, F. Jelezko, R. Laflamme, Y. Nakamura, C. Monroe, and J. L. O'Brien, Nature **464**, 45 (2010).
[3] R. Liu, W. Yao, and L. J. Sham, New J. Phys. **9**, 226 (2007).
[4] G. S. Uhrig, New J. Phys. **10**, 083024 (2008).
[5] R. Roloff, M. Wenin, and W. Pötz, J. Comp. Theor. Nano. **6**, 1837 (2009).
[6] C. Brif, R. Chakrabarti, and H. Rabitz, New J. Phys. **12**, 075008 (2010).
[7] D. A. Lidar and K. B. Whaley, in *Irreversible Quantum Dynamics*, Lecture Notes in Physics, Vol. 622, edited by F. Benatti and R. Floreanini (Springer-Verlag, Berlin, 2003), Chap. 3, pp. 83–120.
[8] P. Zanardi and M. Rasetti, Phys. Rev. Lett. **79**, 3306 (1997).
[9] C. Nayak, S. H. Simon, A. Stern, M. Freedman, and S. Das Sarma, Rev. Mod. Phys. **80**, 1083 (2008).
[10] J. Werschnik and E. K. U. Gross, J. Phys. B: At. Mol. Opt. Phys. **40**, R175 (2007).
[11] G. S. Uhrig, Phys. Rev. Lett. **98**, 100504 (2007).
[12] P. Karbach, S. Pasini, and G. S. Uhrig, Phys. Rev. A **78**, 022315 (2008).
[13] S. Pasini, T. Fischer, P. Karbach, and G. S. Uhrig, Phys. Rev. A **77**, 032315 (2008).
[14] S. Pasini and G. S. Uhrig, J. Phys. A: Math. and Theor. **41**, 312005 (2008).
[15] S. Pasini, P. Karbach, C. Raas, and G. S. Uhrig, Phys. Rev. A **80**, 022328 (2009).
[16] S. Pasini and G. S. Uhrig, J. Phys. A: Math. and Theor. **43**, 132001 (2010).
[17] S. Pasini, P. Karbach, and G. S. Uhrig, Europhys. Lett. **96**, 10003 (2011).
[18] J. P. Palao and R. Kosloff, Phys. Rev. A **68**, 062308 (2003).
[19] A. Messiah, *Quantum Mechanics* (Dover Publications, Inc., New York, 1999).
[20] J. E. Levy, M. S. Carroll, A. Ganti, C. A. Phillips, A. J. Landahl, T. M. Gurrieri, R. D. Carr, H. L. Stalford, and E. Nielsen, New J. Phys. **13**, 083021 (2011).
[21] S. J. van Enk and H. J. Kimble, Quantum Inform. Comput. **2**, 1 (2002).
[22] I. R. Sola and H. Rabitz, J. Chem. Phys. **120**, 9009 (2004).
[23] M. S. Byrd and D. A. Lidar, Phys. Rev. Lett. **89**, 047901 (2002).
[24] M. S. Byrd and D. A. Lidar, Phys. Rev. A **67**, 012324 (2003).
[25] K. Khodjasteh and D. A. Lidar, Phys. Rev. A **68**, 022322 (2003).
[26] H. K. Ng, D. A. Lidar, and J. Preskill, Phys. Rev. A **84**, 012305 (2011).
[27] T. W. Borneman, M. D. Hürlimann, and D. G. Cory, J. Magn. Res. **207**, 220 (2010).
[28] N. Khaneja, T. Reiss, C. Kehlet, T. Schulte-Herbruggen, and S. J. Glaser, J. Magn. Reson. **172**, 296 (2005).
[29] J. S. Li and N. Khaneja, Phys. Rev. A **73**, 030302 (2006).
[30] D. Dong and I. R. Petersen, New J. Phys. **11**, 105033 (2009).
[31] J. Ruths and J. Li, in *49th IEEE Conference on Decision and Control* (IEEE, 2010), pp. 3008–3013.
[32] J. Ruths and J. Li, J. Chem. Phys. **134**, 044128 (2011).
[33] H. K. Cummins and J. A. Jones, New J. Phys. **2**, 6 (2000).
[34] H. K. Cummins, G. Llewellyn, and J. A. Jones, Phys. Rev. A **67**, 042308 (2003).
[35] K. R. Brown, A. W. Harrow, and I. L. Chuang, Phys. Rev. A **70**, 052318 (2004).
[36] W. G. Alway and J. A. Jones, J. Mag. Res. **189**, 114 (2007).
[37] J. Jonathan A., Prog. Nuc. Magn. Res. Spec. **59**, 91 (2011).
[38] W. M. Witzel and S. D. Sarma, Phys. Rev. B **74**, 035322 (2006).
[39] W. M. Witzel, X. Hu, and S. D. Sarma, Phys. Rev B **76**, 035212 (2007).
[40] G. M. Huang, T. J. Tarn, and J. W. Clark, J. Math. Phys. **24**, 2608 (1983).
[41] V. Ramakrishna, M. V. Salapaka, M. Dahleh, H. Rabitz, and A. Peirce, Phys. Rev. A **51**, 960 (1995).
[42] R. Hanson, L. Kouwenhoven, J. Petta, S. Tarucha, and L. Vandersypen, Rev. Mod. Phys. **79**, 1217 (2007).
[43] J. M. Taylor, J. R. Petta, A. C. Johnson, A. Yacoby, C. M. Marcus, and M. D. Lukin, Phys. Rev. B **76**, 035315 (2007).
[44] A. C. Johnson, J. R. Petta, J. M. Taylor, A. Yacoby, M. D. Lukin, C. M. Marcus, M. P. Hanson, and A. C. Gossard, Nature **435**, 925 (2005).
[45] J. R. Petta, A. C. Johnson, J. M. Taylor, E. A. Laird, A. Yacoby, M. D. Lukin, C. M. Marcus, M. P. Hanson, and A. C. Gossard, Science **309**, 2180 (2005).
[46] J. R. Petta, J. M. Taylor, A. C. Johnson, A. Yacoby, M. D. Lukin, C. M. Marcus, M. P. Hanson, and A. C. Gossard, Phys. Rev. Lett. **100**, 067601 (2008).
[47] S. Foletti, H. Bluhm, D. Mahalu, V. Umansky, and A. Yacoby, Nat. Phys. **5**, 903 (2009).
[48] H. Bluhm, S. Foletti, I. Neder, M. Rudner, D. Mahalu, V. Umansky, and A. Yacoby, "Long coherence of electron spins coupled to a nuclear spin bath" (2010), e-print arXiv:1005.2995.
[49] W. Yao, R. B. Liu, and L. J. Sham, Phys. Rev. B **74**, 195301 (2006).
[50] J. E. Levy, A. Ganti, C. A. Phillips, B. R. Hamlet, A. J. Landahl, T. M. Gurrieri, R. D. Carr, and M. S. Carroll, in *Proceedings of the Twenty-First Annual Symposium on Parallelism in Algorithms and Architectures*, SPAA 2009 (ACM, New York, 2009), pp. 166–168.
[51] W. M. Witzel, M. S. Carroll, A. Morello, L. Cywiski, and S. D. Sarma, Phys. Rev. Lett. **105**, 187602 (2010).
[52] R. de Sousa, Phys. Rev. B **76**, 245306 (2007).
[53] J. R. Petta, H. Lu, and A. C. Gossard, Science **327**, 669 (2010).
[54] M. D. Grace, J. Dominy, R. L. Kosut, C. Brif, and H. Rabitz, New J. Phys. **12**, 015001 (2010), Special Issue: Focus on Quantum Control.
[55] M. Grace, C. Brif, H. Rabitz, I. A. Walmsley, R. L. Kosut, and D. A. Lidar, J. Phys. B: At. Mol. Opt. Phys. **40**, S103 (2007), Special Issue on the Dynamical Control of Entanglement and Decoherence.
[56] M. D. Grace, C. Brif, H. Rabitz, D. A. Lidar, I. A. Walmsley, and R. L. Kosut, J. Mod. Opt. **54**, 2339 (2007), Special Issue: 37th Winter Colloquium on the Physics of Quantum Electronics, 2–6 January 2007.
[57] C. A. Fuchs and J. van de Graaf, IEEE Trans. Inf. Theory **45**, 1216 (1999).
[58] J. Dominy and H. Rabitz, J. Phys. A: Math. Theor. **41**, 205305 (2008).
[59] T.-S. Ho, J. Dominy, and H. Rabitz, Phys. Rev. A **79**, 013422 (2009).
[60] G. G. Balint-Kurti, S. Zou, and A. Brown, in *Adv. Chem. Phys.*, Vol. 138, edited by S. A. Rice (John Wiley & Sons, Inc., New York, 2008), pp. 43–94.
[61] V. Jurdjevic and H. J. Sussmann, J. Diff. Eq. **12**, 313 (1972).

[62] C. Brif, R. Chakrabarti, and H. Rabitz, in *Adv. Chem. Phys.*, Vol. 148, edited by S. A. Rice and A. R. Dinner (John Wiley & Sons, Inc., New York, 2012), pp. 1–76.
[63] W. H. Press, B. P. Flannery, S. A. Teukolsky, and W. T. Vetterling, *Numerical Recipes: The Art of Scientific Computing*, 2nd ed. (Cambridge University Press, Cambridge, 1992).
[64] E. Nielsen, R. W. Young, R. P. Muller, and M. S. Carroll, Phys. Rev. B **82**, 075319 (2010).
[65] H. A. Rabitz, M. M. Hsieh, and C. M. Rosenthal, Science **303**, 1998 (2004).
[66] J. Dominy, T. Ho, and H. Rabitz, "Characterization of the critical sets of quantum unitary control landscapes" (2011), e-print arXiv:1102.3502.
[67] A. Rothman, T.-S. Ho, and H. Rabitz, Phys. Rev. A **72**, 023416 (2005).
[68] A. Rothman, T.-S. Ho, and H. Rabitz, J. Chem. Phys. **123**, 134104 (2005).
[69] A. Rothman, T.-S. Ho, and H. Rabitz, Phys. Rev. A **73**, 053401 (2006).
[70] P. T. Boggs and J. W. Tolle, Acta Numerica **4**, 1 (1995).
[71] K. W. Moore, A. Pechen, X. Feng, J. Dominy, V. J. Beltrani, and H. Rabitz, Phys. Chem. Chem. Phys. **13**, 10048 (2011).
[72] A. Donovan, V. Beltrani, and H. Rabitz, Phys. Chem. Chem. Phys. **13**, 7348 (2011).
[73] V. Beltrani, J. Dominy, T.-S. Ho, and H. Rabitz, J. Chem. Phys. **126**, 094105 (2007).
[74] K. W. Moore, R. Chakrabarti, G. Riviello, and H. Rabitz, Phys. Rev. A **83**, 012326 (2011).
[75] V. Guillemin and A. Pollack, *Differential Topology* (Prentice Hall, Englewood Cliffs, New Jersey, 1974).
[76] R. Abraham, J. E. Marsden, and T. Ratiu, *Manifolds, Tensor Analysis, and Applications*, 2nd ed. (Springer-Verlag, New York, NY, 1988).
[77] M. P. do Carmo, *Riemannian Geometry, Mathematics: Theory & Applications* (Birkhäuser, Boston, 1992).
[78] J. W. Milnor, *Topology from a Differentiable Viewpoint, Princeton Landmarks in Mathematics* (Princeton University Press, Princeton, 1997).
[79] A. Uhlmann, Rep. Math. Phys. **9**, 273 (1976).
[80] R. Jozsa, J. Mod. Opt. **41**, 2315 (1994).
[81] K. Khodjasteh and D. A. Lidar, Phys. Rev. Lett. **95**, 180501 (2005).
[82] K. Khodjasteh and D. A. Lidar, Phys. Rev. A **75**, 062310 (2007).
[83] K. Khodjasteh and L. Viola, Phys. Rev. Lett. **102**, 080501 (2009).
[84] K. Khodjasteh and L. Viola, Phys. Rev. A **80**, 032314 (2009).
[85] K. Khodjasteh, D. A. Lidar, and L. Viola, Phys. Rev. Lett. **104**, 090501 (2010).
[86] K. C. Young, D. J. Gorman, and K. B. Whaley, "Fighting dephasing noise with robust optimal control" (2010), e-print arXiv:1005.5418.